



An atomistic-based interphase zone model for crystalline solids

Shaofan Li^{a,*}, Xiaowei Zeng^b, Bo Ren^a, Jing Qian^a, Jinshu Zhang^a, Akhilesh K. Jha^c

^a Department of Civil and Environmental Engineering, University of California, Berkeley, CA 94720, USA

^b Department of Mechanical Engineering, University of Texas, San Antonio, TX 78249, USA

^c NextGen Aeronautics, 2780 Skypark Drive, Suite 400, Torrance, CA 90505, USA

ARTICLE INFO

Article history:

Received 24 December 2011

Received in revised form 9 March 2012

Accepted 23 March 2012

Available online 6 April 2012

Keywords:

Embedded atom method

Finite element method

Fracture

Multiscale simulation

Polycrystalline solids

ABSTRACT

In this paper, we present an atomistic-based interphase zone model (AIZM), discuss its physical foundation, and apply it to simulate fractures at small scales. The main technical ingredients of the atomistic-based multiscale finite element method are: (1) a colloidal crystal model to describe material interface degradation including slip planes, grain boundaries, cracks, and inhomogeneities; (2) implementation of the reduced integration and hour-glass model control technique to avoid locking inside the interphase element, and (3) introduction of a novel concept of “*element stacking fault energy*”, which can be utilized in simulations to distinguish ductile and brittle failures at small scales. In particular, AIZM provides an interface description that is consistent with the bulk material properties, and it can capture microstructure-based mixed-mode interfacial fracture automatically. The method may provide a mesoscale solution for polycrystalline solids by bridging the gap between fine scale molecular dynamics and macroscale continuum dynamics.

© 2012 Elsevier B.V. All rights reserved.

1. Introduction

Fracture is intrinsically a multiscale phenomenon. The phenomenological fracture theory is based on the hypothesis of surface separation or decohesion, which has three independent modes, e.g. Mode-I, II, and III (see Fig. 1 (a)). However, in engineering applications, one often encounter combinations of multiple modes at a single crack site, which we call as the mixed mode fracture. Even though the void growth at mesoscale has been identified as a source for some ductile fractures, cleavage type of surface separation is still regarded as the universal kinematic cracking mechanism when we consider macroscopic fracture. At atomic scale, material failure is characterized as individual atomistic bond breaking, switching (sliding), and interaction transition, e.g. covalent bond becomes colloidal interaction. Hence, cleavage fracture is hardly the only failure mode at small scale. As a matter of fact, one may encounter complex and massive dislocation motions, critical void growth, vacancy formation, grain boundary evolution, localized zigzag surface separation or detachment, intervoid ligament and complex microstructure network, etc. (see [45]). Some of these microscale fracture features may be seen from the result of a simple atomistic simulation shown in Fig. 1(b).

How to relate fracture on these two very different scales and to predict macroscale fracture based on microscale or atomistic scale information is the challenge of contemporary multiscale material science. Recently, several multiscale methods have been devel-

oped, notably the multiscale analysis performed by Horstemeyer et al. [17], the bridging scale method [34], the concurrent electron-to-finite element method [25], and the latest multiscale field theory [8,9,21]. Within the realm of continuum mechanics, there have been some successful methods in prediction of macroscale fracture, one of which is the cohesive zone model (CZM) e.g. [10,27,47,49]. It has achieved much success and popularity in past two decades. However, the conventional cohesive zone model has some limitations:

1. The traction-separation cohesive law adopted is empirical in CZM, and they may be restricted to the condition of small-scale yielding [2,12]. In other words, the conventional cohesive zone model only is suitable for simulations of brittle fractures or quasi-brittle fractures at macroscale.
2. For conventional cohesive zone model to resolve the physical length scale, the size of finite element has to be smaller than the physical cohesive zone length scale i.e. $l_{fem} \leq l_{czm}$. Fail to satisfy such requirement has been the source of mesh-sensitivity of CZM [13].
3. In CZM, the interface cohesive relation is also size-independent. When the defect size becomes very small, say below sub-micron scale, the empirical cohesive law may reach to its limit, because small-scale plasticity is highly size-dependent.
4. In conventional cohesive zone model, the bulk and interface constitutive relations are un-related, therefore in practical engineering applications, it is often difficult to determine the cohesive zone parameter such that the numerical simulation can fit well with experimental results.

* Corresponding author.

E-mail addresses: shaofan@berkeley.edu, li@ce.berkeley.edu (S. Li).

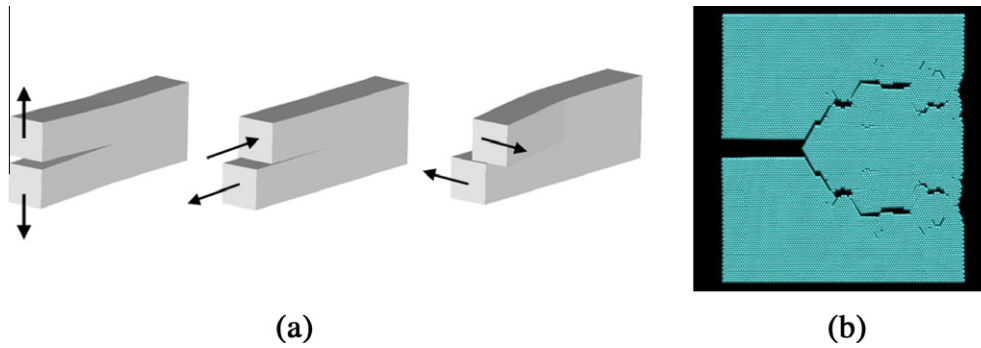


Fig. 1. (a) Macroscale cleavage fracture mode and (b) atomistic scale fracture failure.

5. In the cohesive zone model, the macroscale definition of fracture is adopted i.e. fracture is defined as cleavage of surface separation, and the empirical cohesive law either corresponds to mode-I fracture or to shear mode fracture (mode II or III). A major problem of such approach is that cohesive potentials for different crack modes are difficult to be related, which has been the predicament of requiring an independent criterion for mixed-mode fracture. In crystalline solids, ideally, there should be only one intrinsic fracture criterion that ought to be an essential part of bulk material constitutive relation.
6. In the cohesive zone model, there are two inter-element approaches: (a) the ubiquitous interface approach, in which the boundaries of all inter-elements are taken to be cohesive surface [49], and (b) crack tip approach, in which the cohesive zone is only placed in front of the crack tip [31] (see Fig. 2). Both approaches have their drawbacks: the former alters realistic wave propagation speed, and latter does not have time continuity in cohesive zone formation. Moreover in order to minimize the effect of cohesive zone on bulk elastic stiffness, the element size should be larger than the length scale of the cohesive zone, which conflicts with the requirement that $l_{fem} \leq l_{czm}$ in order to capture size effect of fracture.

To fundamentally resolve all these issues, we need to develop a multiscale CZM in materials science. Recently, there have been discussions in the literature that the cohesive zone model may be salvaged by deriving the cohesive potential from first principle, which has been reflected in [6,24,30]. In [6] the authors have used formal asymptotic and re-normalization group techniques to obtain a coarse-grain or effective cohesive potential for interfacial cohesive

zone. It may be noted that [6] only provide interface normal traction/opening displacement potential, and they did not discuss the shear traction/tangential displacement potential.

To further advance the research on multiscale modeling and simulation of material inhomogeneity, the present authors have proposed a multiscale cohesive zone model (MCZM) in [50,33], which takes a fundamentally different approach on modeling fracture. First instead of viewing the cohesive zone as a virtual interface entity, we consider the cohesive zone as a finite thickness *interphase zone*, in which the deformation, stress, and strain fields are non-uniform. Second, we employ a colloidal crystal analogy to derive the atomistic potential inside the interphase zone, and third, we apply the Cauchy–Born rule to find the effective stress tensor inside the interphase zone.

In this work, we present a systematic study of an atomic-based interphase zone model that is derived from the early multiscale cohesive zone model. In this paper, we have not only cleaned the previous formulation, but also have made the following progress,

1. Provide analysis and justification of the colloidal crystal model that is used to obtain atomistic potential inside interphase elements.
2. Use the Hill–Mandel homogenization method to link the atomistic potential inside the interphase element with the interface traction–separation relation.
3. Use the reduced integration and hour-glass model control techniques to avoid distortion related locking inside interphase elements.
4. Use a novel concept of “*element stacking fault energy*” to study ductile and brittle fracture at small scales.
5. Solve mixed mode fracture problems.
6. Use the multi-body embedded atom potential in AIZM computations.
7. Carry out three-dimensional simulations of fractures at small scale.

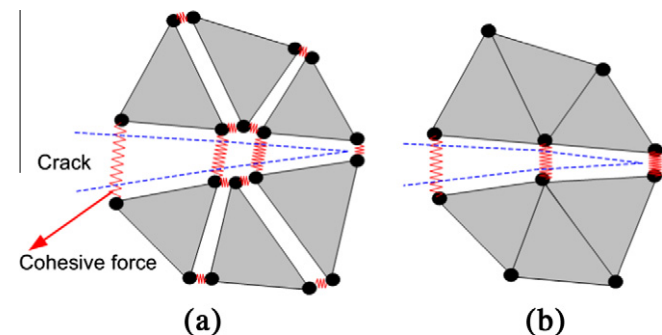


Fig. 2. Inter-element set-up for the conventional cohesive zone model: (a) the ubiquitous approach, and (b) the crack tip approach.

This paper is organized into seven sections: in Section 2 we shall discuss the kinematics of AIZM model, its Galerkin weak formulation, and its finite element implementation; in Section 3 we shall construct the multiscale constitutive models for both bulk elements and interphase elements. In Section 4, we shall discuss how to integrate Galerkin weak form inside the interphase element. In particular, we shall discuss how to avoid distortion induced locking in interphase elements and how to link atomistic potential inside the interphase element with the traction/separation relation along the interface. Section 5 is focused on discussion of element stacking fault energy. In Section 6, six examples of numerical simulations are presented, and finally we shall conclude this study in Section 7.

2. Atomistic multiscale finite element method

Before proceeding to discussion of the AIZM method, we first review two relevant concepts: (1) the Cauchy continuum, and (2) phenomenological cohesive zone model.

2.1. Cauchy continuum

The Cauchy continuum is referred to as a continuum whose deformation is uniform or homogeneous. In this case, the potential energy for a crystalline solid may be calculated by atomistic potential of underline lattice structure based on the so-called Cauchy–Born rule (see Fig. 3)(b). The so-called Cauchy–Born rule is referred to the following procedure: If the deformation in a local region, say in an element, is uniform, the deformation gradient in the region, $\mathbf{F}_e = \frac{\partial \mathbf{x}}{\partial \mathbf{X}}|_{\mathbf{x} \in \Omega_e}$, $e = 1, \dots, n_{elem}$, will be constant. Hence an arbitrarily deformed bond vector \mathbf{r}_i in a unit cell of a given element can be found by mapping the undeformed bond vector \mathbf{R}_i to the deformed vector,

$$\mathbf{r}_i = \mathbf{F}_e \mathbf{R}_i, \quad i = 1, 2, \dots, n_b, \quad (1)$$

where n_b is the total number of bonds in a unit cell. Furthermore, if the deformation in the e th element is uniform, we can calculate the elastic strain energy density in the e th element by calculating the strain energy density of an arbitrary unit cell inside the element,

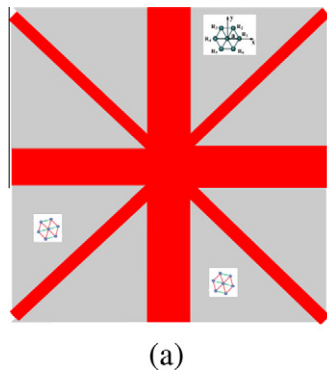
$$W_e = \frac{1}{\Omega_0^u} \sum_{i=1}^{n_b} \phi(r_i) = \frac{1}{\Omega_0^u} \sum_{i=1}^{n_b} \phi(\mathbf{F}_e \mathbf{R}_i) = W_e(\mathbf{F}_e), \quad (2)$$

where $r_i = |\mathbf{r}_i|$. Note that the superscript u indicates the unit cell, and Ω_0^u is the volume of the unit cell in the referential configuration, $\phi(r_i)$ is the atomistic potential, and r_i , $i = 1, 2, \dots, n_b$ are the current bond lengths in a unit cell, where the bond vector \mathbf{r}_i is the distance vector between the center atom in the unit cell to one of the atoms located at a vertex of the unit cell.

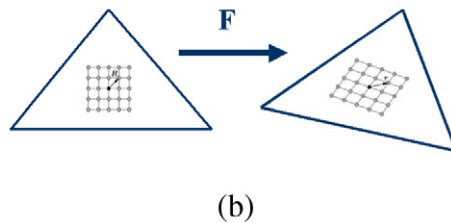
Therefore the deformed bond length is a function of deformation gradient of the element that the unit cell belongs to, i.e. $r_i = |\mathbf{r}_i| = |\mathbf{F}_e \cdot \mathbf{R}_i| = r_i(\mathbf{F}_e)$. Hence, the strain energy density inside each element is the function of the deformation gradient of that element, which can be evaluated at any point inside the element. Consequently, constitutive relations for the bulk medium can be established. For instance, the second Piola–Kirchhoff stress tensor can be obtained in following form,

$$\mathbf{S}(\mathbf{C}) = \frac{1}{\Omega_0^u} \sum_{i=1}^{n_b} \phi'(r_i) \frac{\partial r_i}{\partial \mathbf{C}} = \frac{1}{\Omega_0^u} \sum_{i=1}^{n_b} \frac{\partial \phi}{\partial r_i} \frac{\mathbf{R}_i \otimes \mathbf{R}_i}{r_i}, \quad (3)$$

where $\mathbf{C} = \mathbf{F}_e^T \cdot \mathbf{F}_e$ is the right Cauchy–Green tensor. Similarly, we can find the first Piola–Kirchhoff stress tensor and Cauchy stress tensor in each bulk element as



(a)



(b)

Fig. 3. (a) Kinematic assumption, and (b) the Cauchy–Born rule.

$$\mathbf{P} = \mathbf{F}_e \mathbf{S} = \frac{1}{\Omega_0^u} \sum_{i=1}^{n_b} \frac{\partial \phi}{\partial r_i} \frac{\mathbf{r}_i \otimes \mathbf{R}_i}{r_i}, \quad \text{and} \quad \boldsymbol{\sigma} = J^{-1} \mathbf{F}_e \mathbf{S} \mathbf{F}_e^T = \frac{1}{\Omega^u} \sum_{i=1}^{n_b} \frac{\partial \phi}{\partial r_i} \frac{\mathbf{r}_i \otimes \mathbf{r}_i}{r_i}. \quad (4)$$

The above Cauchy–Born elasticity formulation has been used extensively in many multiscale finite element simulations, when local deformation is considered being uniform.

2.2. Phenomenological cohesive zone model

For the purpose of comparison, we first briefly review the conventional cohesive finite element method. Consider a solid subjected to inhomogeneous deformation that is caused by displacement discontinuity as shown in Fig. 4. In engineering applications, this type of strong discontinuities is the characterization of fracture or dislocations. Initially as a single connected domain, Ω_0 , the body is broken into two disjointed pieces by a cleavage crack. In the referential configuration, the fracture surface, or the plane of division, is denoted as Γ_0 , and it divides the body into two halves: $\Omega_0 = \Omega_0^+ \cup \Omega_0^-$. After the deformation $\boldsymbol{\varphi}$, the body arrives at its deformed or current configuration, Ω (see Fig. 4). We use \mathbf{x} denoting the spatial position of a material point \mathbf{X} at the time t , i.e.

$$\boldsymbol{\varphi} : \Omega_0 \rightarrow \Omega; \quad \mathbf{x} = \boldsymbol{\varphi}(\mathbf{X}) = \mathbf{u} + \mathbf{X}.$$

Two crack surfaces now move to Γ^+ and Γ^- respectively, and the two deformed halves are denoted by Ω^+ and Ω^- . The strong form of the governing equation of the continuum, i.e. the equation of motion, can be written as,

$$\text{DIV} \mathbf{P} + \rho_0 \mathbf{b} = \rho_0 \ddot{\boldsymbol{\varphi}} \quad \text{in } \Omega_0^\pm, \quad (5)$$

$$\boldsymbol{\varphi} = \bar{\boldsymbol{\varphi}} \quad \text{on } \partial_\varphi \Omega_0, \quad (6)$$

$$\mathbf{P} \cdot \mathcal{N} = \bar{\mathbf{T}} \quad \text{on } \partial_t \Omega_0, \quad (7)$$

$$\mathbf{P}^+ \cdot \mathcal{N}^+ + \mathbf{P}^- \cdot \mathcal{N}^- = \mathbf{0} \quad \text{on } \Gamma_0^\pm, \quad (8)$$

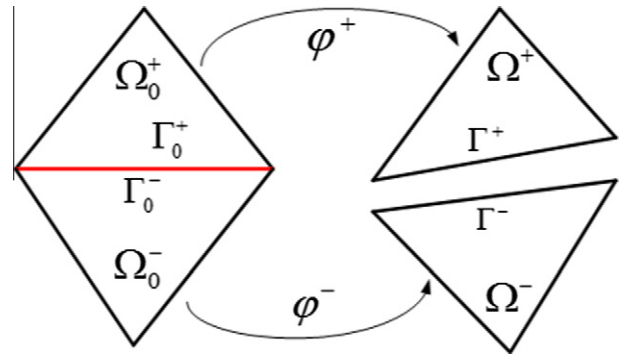


Fig. 4. Illustration of conventional cohesive finite element method.

where \mathbf{b} is the body force, ρ_0 is the mass density in referential configuration. In above equations, the symbol DIV is material divergence operator, i.e. $\nabla_{\mathbf{x}}$, \mathcal{N} is the normal vector of surfaces including the cohesive surface, $\bar{\mathbf{t}}$ is the prescribed traction on $\partial_t \Omega_0$. It is assumed that the traction is continuous along the cohesive surface, Γ_0 , see Eq. (8). For domain boundaries, we denote

$$\partial_\varphi \Omega_0 = \partial_\varphi \Omega_0^+ \cup \partial_\varphi \Omega_0^- \quad \text{and} \quad \partial_t \Omega_0 = \partial_t \Omega_0^+ \cup \partial_t \Omega_0^-, \quad (9)$$

where $\partial_\varphi \Omega$ is the portion of the boundaries where the displacements are prescribed, and $\partial_t \Omega$ is the portion of the boundaries where the traction is prescribed.

In Eqs. (5)–(8), \mathbf{P} is the first Piola–Kirchhoff stress tensor. Considering the constitutive relation of a hyperelastic material, one may find the first Piola–Kirchhoff stress by differentiating the elastic energy density W with respect to deformation gradient,

$$\mathbf{P} = \frac{\partial W}{\partial \mathbf{F}}.$$

Following the standard procedure, we can then derive the Galerkin weak formulation for Eqs. (5)–(8):

$$\begin{aligned} & \int_{\Omega_0^+} \rho_0 \dot{\boldsymbol{\varphi}} \cdot \delta \boldsymbol{\varphi} dV + \int_{\Omega_0^+} \mathbf{P} : \delta \mathbf{F} dV + \int_{\Omega_0^+} \rho_0 \mathbf{b} \cdot \delta \boldsymbol{\varphi} dV \\ & = \int_{\partial_t \Omega_0^+} \bar{\mathbf{T}} \cdot \delta \boldsymbol{\varphi} dS + \int_{\Gamma_0} (\mathbf{P} \cdot \mathcal{N}) \cdot \delta(\boldsymbol{\varphi}^+ - \boldsymbol{\varphi}^-) dS. \end{aligned} \quad (10)$$

The last term in the above equation is the virtual work done by the cohesive traction force across the plane of discontinuity. If we denote the interface displacement jump as:

$$\Delta = \boldsymbol{\varphi}^+ - \boldsymbol{\varphi}^- \quad (11)$$

then we can re-write the last term as:

$$\int_{\Gamma_0} (\mathbf{P} \cdot \mathcal{N}) \cdot \delta(\boldsymbol{\varphi}^+ - \boldsymbol{\varphi}^-) dS = \int_{\Gamma_0} \mathbf{T}^{\text{cohe}} \cdot \delta \Delta dS, \quad (12)$$

where \mathbf{T}^{cohe} denotes the cohesive traction. However, in the theory of phenomenological cohesive zone model, the interface cohesive law is not defined as the projection of the stress, i.e.

$$\mathbf{T}^{\text{cohe}} \neq \mathbf{P} \cdot \mathcal{N} \quad (13)$$

but it is prescribed by an additional interface cohesive potential $W^s(\Delta)$,

$$\mathbf{T}^{\text{cohe}} := \frac{\partial W^s}{\partial \Delta}. \quad (14)$$

The empirical cohesive surface potential, $W^s(\Delta)$, is an independent interface energy potential, which is unrelated to the bulk material property. Moreover the cohesive element between two bulk elements is in fact a zero-thickness virtual element, which has no volume or area associated with it. It has been speculated that the incompatibility between the interface modeling and bulk material modeling may be one of the sources that makes the conventional cohesive zone model solution highly mesh-sensitive or mesh-dependent [13].

Once $W^s(\Delta)$ is chosen, one can calculate cohesive traction along the bulk element boundary. Since $W^s(\Delta)$ is independent from bulk material properties, one may have to make extra effort to select parameters of $W^s(\Delta)$, in order to make it consistent with constitutive relations in the bulk element. Often times, the parameter selection is difficult due to the limitation of fixed functional form of empirical cohesive laws, which do not take into account of complex size effect at small scale.

2.3. Kinematic assumption of AIZM model

In this paper, we present an atomistic-based finite element interphase zone model—a method that is fundamentally different from the conventional cohesive zone model in following ways:

1. Bulk elements undergo uniform deformation, and all the non-uniform deformation is confined inside the interphase elements, i.e. the red region in Fig. 4(a).
2. Fracture is no longer deemed solely as cleavage surface or interface separation but material failure due to a general atomistic debonding in a finite volume.
3. The local material strength is not defined as the threshold of the surface separation but the critical state of the constitutive relation of bulk materials.

It may be noted that traditionally the material strength is considered as the critical state mechanical property of bulk materials, and the use of surface cohesion as the measure of material strength was made popular only after 1960s.

Since our goal is to predict material behaviors at mesoscale, a central question is then: *what is the essential microstructure of defects at mesoscale?*

For crystalline materials, such microstructure is often associated with persistent slip bands, grain boundaries, twin boundaries, stacking faults, etc. Based on this observation, we adopt the following kinematic assumptions.

The deformation inside every bulk element is uniform or homogeneous, whereas all defect caused non-uniform deformations are confined inside the interphase element, which is a narrow finite thickness strip that is either along the slip planes, grain boundaries, or twin boundaries. This kinematic assumption is really a reminiscence of the kinematic assumption of crystal plasticity [44], which has been widely accepted and recognized as one of the best meso-mechanics models for polycrystalline solids. Similar kinematics assumption is adopted in the Peierls–Nabarro dislocation model [35,29], in which outside the finite thickness interphase zone, the material is modeled as linear elastic, whereas inside the finite thickness interphase zone the deformation is highly non-linear. We may note in passing that a key difference between the proposed AIZM model and conventional CZM is that in AIZM the interphase element is a real, finite size element, whereas the conventional cohesive zone element is a virtual, zero-thickness interface entity (see Fig. 5(a)).

2.4. Galerkin variational weak formulation of AIZM

In the following, we present the Galerkin variational weak formulation of the proposed AIZM method. Denote the domain of interests in the reference configuration as Ω_0 . In two-dimensional space, we can discretize it in a set of disjointed triangle bulk elements, Ω_b^e , $e = 1, 2, \dots, n_{elem}^b$, and a set of disjointed quadrilateral interphase element Ω_c^i , $i = 1, 2, \dots, n_{elem}^c$, such that

$$\Omega_0 = \left(\bigcup_{e=1}^{n_{elem}^b} \Omega_b^e \right) \cup \left(\bigcup_{i=1}^{n_{elem}^c} \Omega_c^i \right). \quad (15)$$

Note that mathematically or topologically the set of triangle elements and quadrilateral elements may not be able to form a compact cover of Ω_0 , because there could be a tiny hole in the vertex of the triangle elements, if all the elements are within the same scale. Nevertheless, Eq. (15) is essentially a physical statement rather than a mathematical statement. We may interpret the AIZM mesh as a multiscale mesh, which means that at macroscale the set of triangle elements forms a mathematical cover of Ω_0 , but zooming in the fine scale one may find an interphase quadrilateral layer

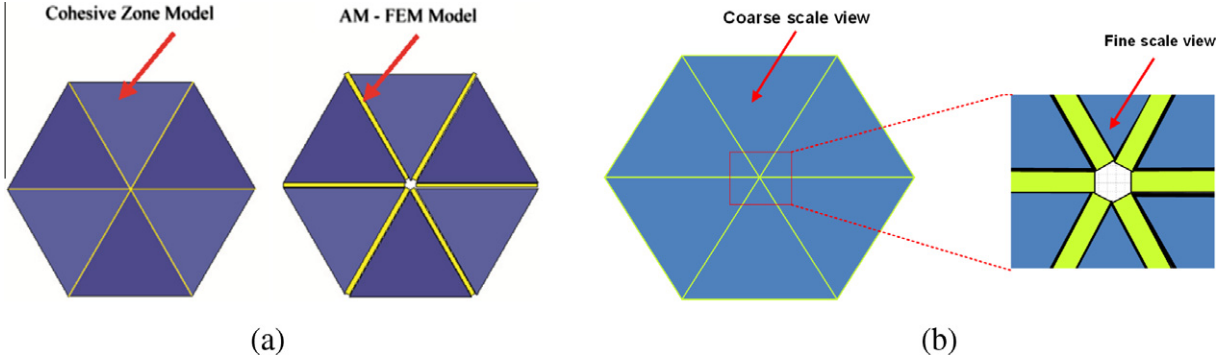


Fig. 5. (a) Comparison between regular CZM and AIZM, and (b) multiscale interpretation of AIZM mesh.

between two adjacent macroscale triangle elements (Fig. 7(b)). Moreover, at the vertex of six bulk elements and six interphase elements, there is actually a six-node hexagonal fifth order finite element. In most numerical examples reported in this paper, the contribution of the hexagonal element is negligible, because the ratio of the thickness of the interphase element, R_0 , and the characteristic length of the bulk element, ℓ_{fem} , is very small, i.e. $R_0/\ell_{fem} < 10^{-2}$. If, however, $R_0/\ell_{fem} \rightarrow \mathcal{O}(1)$, the contribution from this term will become significant. This is usually the case when one tries to scale down AIZM to atomic scale, and we shall study this case in a separate paper.

With the aid of trail function φ^h and test function $\delta\varphi^h$, a Lagrangian type of Galerkin Lagrangian weak formulation may be expressed as follows,

$$\begin{aligned} & \sum_{e=1}^{n_b^{elem}} \left\{ \int_{\Omega_b^e} \rho_0 \dot{\varphi}^h \cdot \delta\varphi^h dV + \int_{\Omega_b^e} \mathbf{P}(\varphi) : \delta\mathbf{F}^h dV \right\} \\ & + \sum_{i=1}^{n_c^{elem}} \left\{ \int_{\Omega_c^i} \rho_0 \dot{\varphi}^h \cdot \delta\varphi^h dV + \int_{\Omega_c^i} \mathbf{P}(\varphi) : \delta\mathbf{F}^h dV \right\} \\ & = \sum_{e=1}^{n_b^{elem}} \left\{ \int_{\Omega_b^e} \rho_0 \mathbf{b} \cdot \delta\varphi^h dV + \int_{\partial_t \Omega_b^e} \bar{\mathbf{T}} \cdot \delta\varphi^h dS \right\} + \sum_{i=1}^{n_c^{elem}} \int_{\Omega_c^i} \rho_0 \mathbf{b} \cdot \delta\varphi^h dV, \end{aligned} \quad (16)$$

where \mathbf{b} is the body force, Ω_b^e is the e th bulk element, $\partial_t \Omega_b^e$ is the interception between the traction boundary and the boundary of the e -th element, and Ω_c^i is the i th interphase element. The interphase element does not overlap with traction boundary $\partial_t \Omega_b$. The interphase element is a narrow quadrilateral strip with side aspect ratio, $R_0/\ell_{fem} = 10^{-5} \sim 10^{-2}$. Integration by parts, one may approxi-

mate the volume integral of the i th interphase element as a pair of surface integrals,

$$\int_{\Omega_c^i} \mathbf{P} : \delta\mathbf{F} dV \approx \int_{\Gamma_c^{i+}} \mathbf{P} \cdot \mathcal{N} \cdot \delta\varphi dS + \int_{\Gamma_c^{i-}} \mathbf{P} \cdot \mathcal{N} \cdot \delta\varphi dS. \quad (17)$$

Note that the boundary integrations over the two short sides of quadrilateral are neglected, and this is because first R_0/L_0 is very small, and second they will be canceled by the boundary integrals from the adjacent interphase elements if we sum the total contribution from all interphase elements.

Let $\mathcal{N}^+ = -\mathcal{N}^- = \mathcal{N}$. We may then write,

$$\int_{\Omega_c^i} \mathbf{P} : \delta\mathbf{F} dV \approx \int_{\Gamma_c^{i+}} \mathbf{P} \cdot \mathcal{N} \cdot \delta(\varphi^+ - \varphi^-) dS = \int_{\Gamma_c^+} \mathbf{T}_c^i \cdot \delta\Delta dS. \quad (18)$$

The difference between Eqs. (18) and (12) is that we evaluate \mathbf{T}^i by directly calculating,

$$\mathbf{T}_c^i := \mathbf{P} \cdot \mathcal{N} \quad \text{and} \quad \delta\Delta := \delta(\varphi^+ - \varphi^-) \quad (19)$$

instead of utilizing empirical interface cohesive potential. In Eq. (19), \mathbf{P} is the 1st Piola–Kirchhoff stress inside the interphase element, which is determined by the atomistic enriched constitutive relation inside interphase elements.

Remark 2.1.

- I. In computations, we use the row-sum technique to calculate the lump mass for each FEM node. Fig. 6 shows a bulk element/interphase element unit, in which a FEM node will receive 1/3 of the mass from the triangle bulk element, and receive $2 \times 1/4$ of mass of the interphase element from

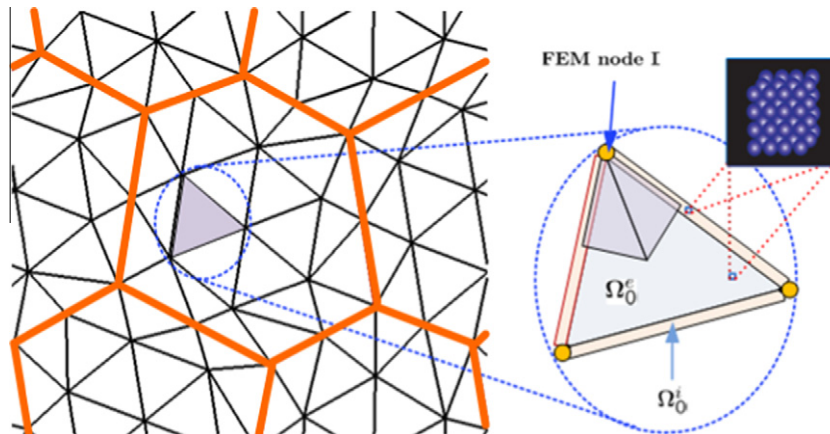


Fig. 6. Atomistic-based multiscale finite element discretization.

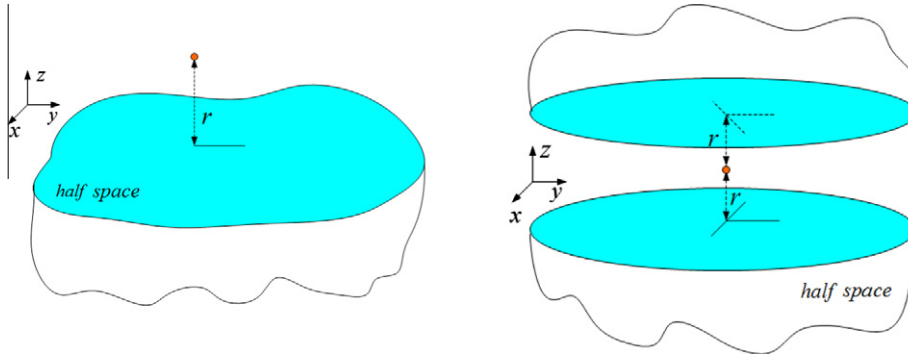


Fig. 7. Modeling of atomistic potential inside the interphase element.

the two adjacent interphase elements. Since this is a Lagrangian method, after the interphase element fails, the mass of the FEM system remains conserved.

II. It is worth noting the subtle differences between Eqs. (16) and (10). Because of having a finite-thickness interphase zone, the AIZM does not need or use the jump operator to describe discontinuous displacement field, which has been employed in the conventional cohesive finite element method and the extended finite element (X-FEM). This difference will be reflected in the implementation of Galerkin finite element formulation of the AIZM. In most of calculations done in this work, we simply integrate the volume integral by using the reduced integration technique.

2.5. FEM implementations

Consider following FEM interpolation in each element,

$$\mathbf{u}^h(\mathbf{X}) = \sum_{I=1}^{n_{\text{node}}} N_I(\mathbf{X}) \mathbf{d}_I. \quad (20)$$

Following the standard FE discretization procedure, e.g. [5,19], we have the following discrete equations of motion

$$\mathbf{M} \ddot{\mathbf{d}} + \mathbf{f}^{\text{int}}(\mathbf{d}) = \mathbf{f}^{\text{ext}}, \quad (21)$$

where

$$\mathbf{M} = \mathcal{A} \int_{B_0^e} \rho_0 \mathbf{N}^e \mathbf{T} \mathbf{N}^e dV + \mathcal{A} \int_{B_0^i} \rho_0 \mathbf{N}^i \mathbf{T} \mathbf{N}^i dV, \quad (22)$$

$$\mathbf{f}^{\text{int}} = \mathcal{A} \int_{B_0^e} \mathbf{B}^e \mathbf{T} \mathbf{P}^e(\mathbf{d}) dV + \mathcal{A} \int_{B_0^i} \mathbf{B}^i \mathbf{T} \mathbf{P}^i(\mathbf{d}) dV, \quad (23)$$

$$\mathbf{f}^{\text{ext}} = \mathcal{A} \int_{B_0^e} \mathbf{N}^e \mathbf{T} \rho_0 \mathbf{b} dV + \int_{\partial_t B_0^e} \mathbf{N}^e \mathbf{T} \bar{\mathbf{T}}^e dS \left\} + \mathcal{A} \int_{B_0^i} \mathbf{N}^i \mathbf{T} \rho_0 \mathbf{b} dV, \quad (24)$$

where \mathcal{A} is the element assemble operator, \mathbf{N}^e and \mathbf{N}^i are element shape function matrices for bulk elements and interphase elements, and \mathbf{B}^e and \mathbf{B}^i are element B-matrices for bulk elements and interphase elements respectively.

The explicit time integration based Newmark- β method with $\beta = 0$ [3] is used in the displacement update,

$$\mathbf{d}_{n+1} = \mathbf{d}_n + \mathbf{v}_n \Delta t_n + \frac{1}{2} \mathbf{a}_n (\Delta t_n)^2, \quad (25)$$

$$\mathbf{a}_{n+1} = \mathbf{M}^{-1} (\mathbf{f}^{\text{ext}} - \mathbf{f}^{\text{int}}), \quad (26)$$

$$\mathbf{v}_{n+1} = \mathbf{v}_n + \frac{1}{2} (\mathbf{a}_n + \mathbf{a}_{n+1}) \Delta t_n, \quad (27)$$

where \mathbf{d}_n is the displacement field at the time step n , \mathbf{v}_n is the velocity field at the time step n , and \mathbf{a}_n is the acceleration field at the time

step n . The subscript n and $n + 1$ denote to quantities evaluated at time t_n and t_{n+1} .

3. Constitutive modeling of AIZM

There are two types of elements in the atomistic-based interphase zone model: the bulk element and the interphase element. Since the deformation inside the bulk element is assumed to be homogeneous, it can be simply modeled as a Cauchy continuum, and its constitutive relation may be obtained by directly applying the Cauchy–Born rule (see Eqs. (3) and (4)). On the other hand, the constitutive modeling the interphase zone is more involved. The interphase zone is employed to model both slip line inside the single crystal as well as the grain boundaries between different single crystal grains. Nevertheless, the constitutive modeling of these two different cases are different. For the interphase zone representing existing grain boundary, we employ a colloidal crystal interphase model; and for the interphase zone inside the single crystal we adopt an asymptotic colloidal crystal interphase model.

3.1. Colloidal crystal interphase model

To model material damage process at sub-mesoscale or meso-scale, we propose to treat the interphase as a type of colloidal crystal, or a partially colloidal crystal. The advantage and justification of modeling the interphase zone as a colloidal crystal are: (1) it reflects the presence of vacancy population inside the interphase zone, and (2) as have been shown in the literature, e.g. [42,43], the colloidal crystal model can capture some basic features of crystalline material failure process such as defect nucleation, and thermal fluctuation.

In this work, the colloidal crystal modeling of material interphase is referred to as the following procedure: We mix a van der Waals type of intermolecular adhesive force with atomistic covenant bond force to model the interatomic interaction inside interphase elements. In colloidal physics, the van der Waals cohesive force along the surface has been traditionally characterized as the *depletion potential* in contrast to interatomic potential in the bulk materials. In this paper, we borrow the phrase *depletion potential* from colloidal physics in the sense that this denotes a coarse-grain molecular potential in the interphase element. In physical reality, there are still lattice microstructure inside grain boundaries, twin or phase boundaries, and stacking faults. However, the atomistic bonding situation or electron density distribution inside those interphases is complex; and there are metallic, ionic, or even covalent bonding as well as van der Waals interactions inside physical interphases between different grains, these bonds may have low cohesive energies because they may be associated with segregant atoms and large population of vacancy. Therefore a

colloidal crystal approach is pertinent to characterization of the cohesion or decohesion mechanism inside the interphase element.

To obtain the depletion potential in a weak interphase zone, we assume that the interphase element is much softer than the adjacent bulk elements, and the intermolecular interaction inside the interphase zone may be treated as a quasi-Van der Waals interaction that can be linearly superposed. In fact, we may view the bulk medium as rigid with almost no deformation, so the two bulk elements adjacent to the compliant interphase zone may be viewed as two rigid body half spaces (see Fig. 7). If the atomistic potential for a given bulk medium is available, which can be a pair potential, an EAM (embedded atom method) type potential [11], or any other atomistic potentials, we can obtain the depletion potential in the interphase element by integrating the bulk potential over two bulk medium half spaces. In general, the interphase depletion potential may be obtained by following analytical integration (e.g. [20], pp. 156–158),

$$\phi_{depl}(r) = \int_{\text{Half Space}} \beta \phi_{bulk}(r-r') dV', \quad (28)$$

where β is parameter related to normalized atom density.

Some interphase depletion potentials may even have close form expressions. For example, if the Lennard-Jones (LJ) potential is chosen as the bulk potential as,

$$\phi_{bulk} = 4\epsilon \left(\left(\frac{\sigma}{r}\right)^{12} - \left(\frac{\sigma}{r}\right)^6 \right) \quad (29)$$

the corresponding interphase depletion potential will be (see [41])

$$\phi_{depl} = \frac{\pi\epsilon}{\sqrt{2}} \left(\frac{1}{45} \left(\frac{r_0}{r}\right)^9 - \frac{1}{3} \left(\frac{r_0}{r}\right)^3 \right), \quad (30)$$

where ϵ is the depth of the potential well, and σ is the (finite) distance at which the bulk atomistic potential is zero. $r_0 = \sigma 2^{1/6}$ is the equilibrium bond distance in the bulk material.

If the materials adjacent to the interphase are different, $\phi_{depl}^1 \neq \phi_{depl}^2$, we assume that the interphase atomistic potential is the average of depletion potentials in two adjacent half spaces.

$$\phi_{depl} = \frac{1}{2} (\phi_{depl}^1 + \phi_{depl}^2). \quad (31)$$

If the material in both elements are the same, we have $\phi_{intp} = \phi_{depl}$. This approach is mainly used to model grain boundary, twin boundary, existing slip band, and interphase of composite materials.

It should be noted that there is a fundamental difference between the approach adopted in conventional cohesive zone model and the depletion potential approach adopted in this work. In conventional CZM, the cohesive potential is a potential of interface traction and separation, whereas the depletion potential derived here is “a volumetric intermolecular potential”. Moreover, the depletion potential proposed in this work is a coarse-grained interphase potential model, which is not the same as the depletion potential in chemical physics.

3.2. Asymptotic colloidal crystal interphase model

For interphase zones inside a single crystal, we take a slight different approach, which is termed as the asymptotic colloidal crystal interphase model. In this case, we first consider the interphase element and the bulk element have the same material properties at the beginning, i.e. initially the atomistic potential inside the interphase element is exactly the same as the atomistic potential inside the bulk element. When the internal stress increases to certain level, we postulate that the material may start to degrade, and inhomogeneous deformation starts to build up inside the thin slice of the interphase zone.

In the simulation, we choose the following asymptotic and mixed atomistic potential inside the interphase zone,

$$\phi_{intp}(r) = \begin{cases} \phi_{bulk}(r), & r < r^*, \\ \alpha \phi_{bulk}(r) + (1 - \alpha) \phi_{depl}(r), & r \geq r^*; \end{cases} \quad (32)$$

where r^* is a bond distance at which, $\phi'_{bulk}(r^*) = \phi'_{depl}(r^*)$ (see Fig. 8), $0 \leq \alpha \leq 1$ is a material parameter.

Without loss of generality, we illustrate the proposed constitutive modeling of the interphase element by using the following two-dimensional example. For illustration purpose, the AIZM model may be simplified as two triangle bulk elements sandwiching one quadrilateral interphase element (see Fig. 8 (a)). To demonstrate how AIZM works, we may simplify the combination of the two bulk triangle elements/one interphase quadrilateral element as a one-dimensional model of three-spring in series connection; the two red springs representing two bulk elements are at top and bottom, and the blue spring representing the interphase element is in the middle of the series spring connection (see Fig. 8(a)).

In Fig. 8(b), we then plot the force–displacement relations inside the interphase element with different values of α . At the

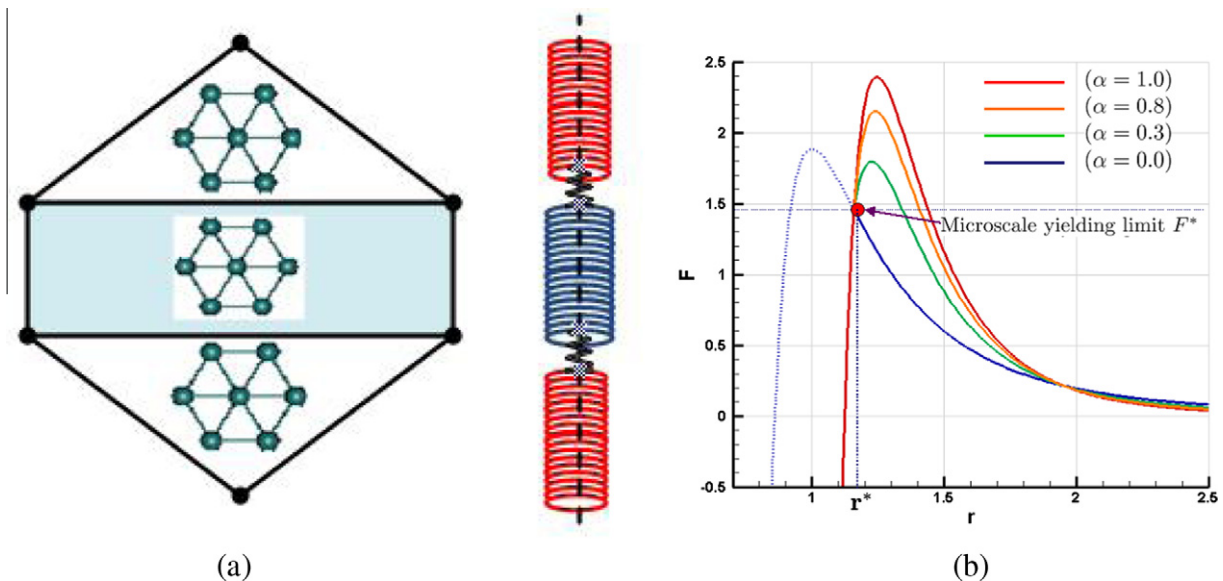


Fig. 8. (a) Two bulk elements sandwich an interphase element, and (b) atomistic force–displacement relation inside interphase elements ($\phi_{intp} = \alpha \phi_{bulk} + (1 - \alpha) \phi_{depl}$).

beginning, when bond distance $r < r^*$, both the bulk element and the interphase element have the same atomistic potential (the red line). When $r \rightarrow r^*$, the force inside all three springs will reach to F^* . If we continues to stretch the bond length, the interphase element will start to unload ($\alpha = 0$), which follows the blue path, whereas the bulk elements will also be in an unloading state, but they will stay in the red path ($\alpha = 1.0$) below the point F^* .

Therefore as the material continues to stretch, the bond length inside the interphase element will increase significantly until it breaks while the bulk elements remain in a uniform deformation state, in which the force–displacement relation is almost linear elastic.

Remark 3.1. First from Fig. 8 one may observe that no matter what the value of α is, the atomistic potential inside the interphase element will always start at the same point (r^* , F^*), which we label it as the *Microscale yielding limit*. Since this point is solely determined as the interception between the depletion potential and the original atomistic potential, it may be regarded as a material parameter. When $\alpha = 0$, after this point, the interphase element starts moving on a softening path; when $\alpha \neq 0$, the interphase element may experience some microscale hardening, which resembles the macroscale material behavior. Second the value microscale yielding may be controlled by the normalized atom density parameter β , which may be related to the porosity or vacancy density in the interphase element. Third if $\alpha = 1.0$, then $\phi_{intp} = \phi_{bulk}$, which is the case that there is basically no material degradation in the interphase element. The proposed AIZM method will still work in case with additional kinematic constraints on interphase elements, and most of the results that have been presented in this paper are valid in this case, if we enforce the stability constraints on the interphase element. Interested readers may consult a recent work that is entirely done by taking $\alpha = 1.0$ [15].

3.3. Material strength inside the interphase element

An important technical ingredient of the proposed atomistic-based multiscale finite element model is how to derive stress–strain relation based on the depletion potential inside the interphase element, in which the deformation is inhomogeneous. One may assume that displacement field inside interphase element may be decomposed into two different scales,

$$\mathbf{x} = \mathbf{X} + \bar{\mathbf{u}}(\mathbf{X}) + \mathbf{u}'(\mathbf{X}) = \bar{\mathbf{x}} + \mathbf{u}',$$

where $\bar{\mathbf{u}}$ represents the coarse scale displacement field, which is assumed to be determined by finite element interpolation field, and \mathbf{u}' is the fine scale displacement field that the FEM interpolation field may not be able to capture. Consequently, we have

$$\mathbf{F} = \frac{\partial \mathbf{x}}{\partial \mathbf{X}} = \frac{\partial \bar{\mathbf{x}}}{\partial \mathbf{X}} + \frac{\partial \mathbf{u}'}{\partial \mathbf{X}} = \bar{\mathbf{F}} + \mathbf{F}',$$

where \mathbf{F}' is the fine scale deformation.

The ability of an interphase element to capture nonlinear deformation depends on the order of its interpolation function. In this paper, we only use the quadrilateral element (2D) and the wedge element (3D) to model interphase zone. To capture nonlinear deformation inside the interphase zone such as strain gradient effect, we have employed high order bubble mode to enrich interpolation displacement field, and we shall report the detailed FEM implementation in a separate paper. Even though within the interphase element, the deformation is non-uniform, to establish stress–strain relation inside the interphase zone we assume that the stress state inside the interphase element only depends on the local homogeneous displacement field surrounding each quadrature point. By doing so, we can apply the Cauchy–Born rule at each quadrature point inside the interphase element, i.e.

$$W_{qp} = \frac{1}{\Omega_u} \sum_{i=1}^{n_b} \phi_{intp}(\bar{\mathbf{F}} \cdot \mathbf{R}_i) = W_{qp}(\bar{\mathbf{F}}(\mathbf{X})).$$

Then the stress at each quadrature point can be obtained as

$$\mathbf{S} = \frac{1}{\Omega_u} \sum_{i=1}^{n_b} \frac{\partial \phi_{intp}}{\partial r_i} \frac{\mathbf{R}_i \otimes \mathbf{R}_i}{r_i} = \mathbf{S}(\mathbf{X}),$$

where the spatial dependence on \mathbf{X} is due to the fact $\mathbf{r}_i \approx \bar{\mathbf{F}}(\mathbf{X}_{qp}) \cdot \mathbf{R}_i$. Consider the following FEM interpolation inside the interphase element,

$$\bar{\mathbf{u}}(\mathbf{X}) = \sum_{l=1}^{n_c^{node}} N_l(\mathbf{X}) \mathbf{d}_l$$

and

$$\bar{\mathbf{F}}_{qp} = \sum_{l=1}^{n_c^{node}} \mathbf{x}_l \otimes \frac{\partial N_l(\mathbf{X}_{qp})}{\partial \mathbf{X}},$$

where n_c^{node} is the total number of FEM nodes in an interphase element, and \mathbf{x}_l is the element nodal position. In contrast to the bulk element, the stress field inside the interphase element is non-uniform because for quadrilateral elements $\partial N_l / \partial X$ is not constant.

4. Quadrature in interphase elements and interface traction–separation relation

Computationally, AIZM model is not a variant of element deletion algorithm, but a natural (automatic) element dislocation and disintegration algorithm that is controlled by intrinsic material strength inside the interphase zone. To ensure such element dislocation/disintegration corresponding to real material failure phenomena, one has to make sure that there is no numerical mishandling. Moreover, we hope to relate such physical process at microscale with what have been observed at macroscale. In fact, the proposed AIZM method is similar to the so-called virtual internal bond (VIB) method [14] in certain aspects. However, without adopting the interphase zone and using the depletion potential inside, we have found that the computational model is both physically and numerically unstable, which is probably a main shortcoming of VIB method.

4.1. Reduced integration and hour-glass control for interphase elements

As mentioned before, the interphase element is constructed as a narrow strip; for example it may be a slender four-node quadrilateral element (2D), or a thin layer six-node wedge element (3D). For both elements, they have a finite but very small thickness R_0 . The thickness of the interphase element, R_0 , is a physical parameter that is related to the characteristic length scale of specific defects under consideration. Let ℓ_{fem}^{\pm} be the characteristic length of the bulk element. We choose $10^{-5} |\ell_{fem}^{\pm}| \leq R_0 \leq 10^{-2} |\ell_{fem}^{\pm}|$. The large aspect ratio of ℓ_{fem} / R_0 could cause the interphase element exhibits shear locking during large deformation, which is always the case when an interphase element fails.

To solve the problem, a reduced integration technique is adopted to alleviate the element locking caused by severe element distortion during the element disintegration. On the other hand, it is well known that the straight-forward reduced integration may cause spurious hour-glass mode, which may produce spurious crack morphology such as inter-element penetration. Therefore, the reduced integration technique may have to be used in combination with hourglass mode control measure. In the literature, there are several hour-glass mode control strategies, such as selective reduced integration (SRI) [4,26].

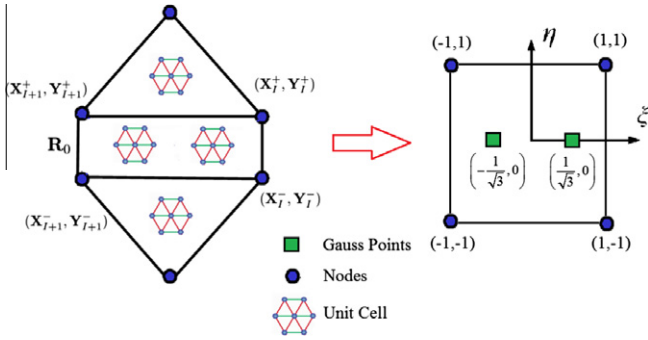


Fig. 9. Illustration of the reduced integration for quadrilateral interphase element.

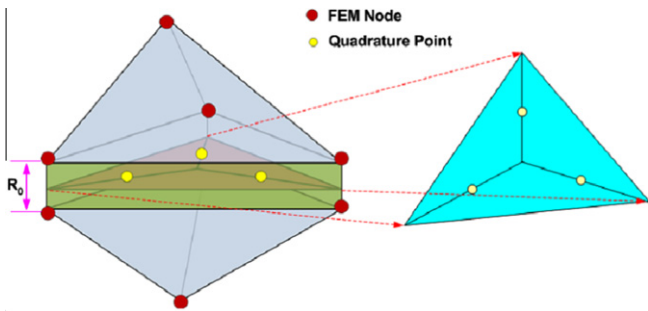


Fig. 10. Illustration of the reduced integration for three-dimensional interphase wedge element: (a) bulk-interphase element sandwich, and (b) quadrature point distribution on the middle plane of the interphase element.

A systematic study on how to apply reduced integration/hour-glass mode control technique to correctly simulate interphase element failure is still in progress. Here we report two reduced integration techniques that may not need hour-glass mode control measure.

First for 2D quadrilateral interphase element, we have used two-point reduced integration technique to successfully avoid hour-glass mode during fracture simulation. The two-point reduced integration scheme is illustrated in Fig. 9. Second, in a similarly way, we have used a three-point reduced integration for 3D 6-node wedge shape interphase element, which is sandwiched by two tetrahedral bulk elements. The three-point integration algorithm is demonstrated in Fig. 9. We placed the three quadrature points at the middle plane of the wedge element at three locations where the distance from the center of the triangle equals to the distance from one of the vertices of the middle triangle. We have used the three-point reduced integration algorithm in 3D calculation, and it provides better results than the one-point integration algorithm or static condensation technique.

4.2. Static condensation and interface cohesive law

In principle, the proposed AIZM is fundamentally different from the conventional cohesive zone model (CZM) both in physical principle as well as computational algorithm. This is because that CZM is essentially based on a postulate of macroscale fracture mechanics that *fracture is a cleavage surface separation with a process zone in front of the crack tip*; whereas in the proposed AIZM model, we do not adopt such hypothesis any more. However, one may interpret the AIZM as an atomistic-based multiscale cohesive zone model by using an equivalent traction/separation law obtained by the static condensation to convert a volumetric stress/strain relation to a surface traction/separation relation.

The procedure of “the static condensation” is first calculating effective deformation gradient inside the interphase element, and then find the average stress by applying the Cauchy–Born rule to the effective deformation field, and finally project the average stress into the boundary between the interphase element and the bulk element, which will automatically provide an interface cohesive traction-separation relation.

A popular computational homogenization technique is to represent the general deformation field as

$$\mathbf{x} \approx \bar{\mathbf{F}}^c \cdot \mathbf{X} + \mathbf{u}', \quad (33)$$

where $\langle \mathbf{F} \rangle_c$ is a constant two-point tensor that can be determined by the boundary data along interphase elements,

$$\bar{\mathbf{F}}^c = \frac{1}{|\Omega_0|} \int_{\Omega_0} \frac{\partial \mathbf{x}}{\partial \mathbf{X}} = \frac{1}{|\Omega_0|} \int_{\partial \Omega_0} \mathbf{x} \otimes \mathcal{N} dS. \quad (34)$$

Since the deformation inside bulk elements is uniform, it is reasonable to assume that $\mathbf{u}' \equiv 0$ along the boundary of bulk elements. Since the boundary of each interphase zone shares the same boundary with the adjacent bulk elements, on the boundary of each interphase element the fine scale fluctuation displacement field should vanish as well. This fact implies that $\mathbf{u}' = 0, \forall \mathbf{X} \in \partial_t \Omega_e$, $e = 1, 2, \dots, N_{elem}$ which stems from the basic kinematic assumption of AIZM. Similar assumption was also adopted in Taylor’s crystal plasticity and the Peierls–Nabarro theory. Hence, the following weak condition for fine scale displacement,

$$\int_{\partial \Omega_c} \mathbf{u}' \otimes \mathcal{N} dS = 0 \quad (35)$$

should be held automatically. That is: $\mathbf{x} = \bar{\mathbf{x}}, \forall \mathbf{X} \in \partial \Omega_0$. Hence we can determine the affine deformation map, $\bar{\mathbf{F}}^c$, if we know finite element nodal displacement. For example, in the case of plane strain, for a given FEM nodal point along the boundary of the interphase element

$$\bar{x}_1 = a_1 + \bar{F}_{11}^c X_1 + \bar{F}_{12}^c X_2, \quad (36)$$

$$\bar{x}_2 = a_2 + \bar{F}_{21}^c X_1 + \bar{F}_{22}^c X_2, \quad (37)$$

$$\bar{x}_3 = a_3 + X_3, \quad (38)$$

where \bar{F}_{ij}^c are constants.

Consider the plane strain case as an example and fix the rigid body motion $a_1 = a_2 = a_3 = 0$. One can easily determine the effective deformation gradient $\bar{\mathbf{F}}^c$ by using the information of FEM nodal displacements. For example, we can use the deformations of two diagonal lines of the interphase zone, which can be expressed by the FEM nodal displacements,

$$\mathbf{x}_{I+1}^+ - \mathbf{x}_I^- = \bar{\mathbf{F}}^c \cdot (\mathbf{X}_{I+1}^+ - \mathbf{X}_I^-), \quad \text{and} \quad \mathbf{x}_I^+ - \mathbf{x}_{I+1}^- = \bar{\mathbf{F}}^c \cdot (\mathbf{X}_I^+ - \mathbf{X}_{I+1}^-) \quad (39)$$

to explicitly determine the effective deformation gradient $\bar{\mathbf{F}}^c$ inside the interphase zone as follows (see Fig. 11):

$$\begin{bmatrix} \bar{F}_{11}^c \\ \bar{F}_{12}^c \\ \bar{F}_{21}^c \\ \bar{F}_{22}^c \end{bmatrix} = \frac{1}{(ad - cb)} \begin{bmatrix} d & 0 & -b & 0 \\ -c & 0 & a & 0 \\ 0 & d & 0 & -b \\ 0 & -c & 0 & a \end{bmatrix} \begin{bmatrix} x_{I+1}^+ - x_I^- \\ y_{I+1}^+ - y_I^- \\ x_I^+ - x_{I+1}^- \\ y_I^+ - y_{I+1}^- \end{bmatrix}, \quad (40)$$

where

$$a = X_{I+1}^+ - X_I^-, b = Y_{I+1}^+ - Y_I^-, c = X_I^+ - X_{I+1}^-, d = Y_I^+ - Y_{I+1}^-. \quad (41)$$

In fact, the above procedure is a multiscale version of the Hill–Mandel homogenization (see [16,23]). Adopting the assumption,

$$\mathbf{x} \approx \bar{\mathbf{F}}^c \mathbf{X} + \mathbf{u}'$$

and hence the 1st Piola–Kirchhoff stress tensor at any point inside the interphase element may be evaluated as,

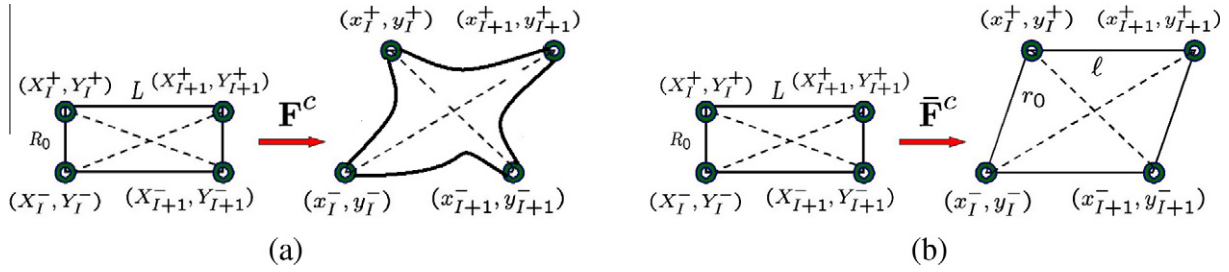


Fig. 11. (a) Deformation inside the interphase element, and (b) average deformation in the interphase element.

$$\mathbf{P} = \frac{\partial W}{\partial \mathbf{F}} \approx \frac{\partial W}{\partial \mathbf{F}^c} + \frac{\partial^2 W}{\partial \mathbf{F}^c \partial \mathbf{F}^c} : \left(\frac{\partial \mathbf{u}'}{\partial \mathbf{X}} \right) + \mathcal{O} \left(\left| \frac{\partial^2 \mathbf{u}'}{\partial \mathbf{X}^2} \right| \right). \quad (42)$$

The average 1st Piola–Kirchhoff stress tensor in an interphase element may be approximated as

$$\langle \mathbf{P} \rangle := \bar{\mathbf{P}}^c = \frac{1}{|\Omega_0|} \int_{\Omega_0} \mathbf{P} d\Omega \approx \frac{\partial W}{\partial \mathbf{F}^c} + \frac{\partial^2 W}{\partial \mathbf{F}^c \partial \mathbf{F}^c} : \left(\frac{1}{|\Omega_0|} \int_{\Omega_0} \frac{\partial \mathbf{u}'}{\partial \mathbf{X}} d\Omega \right) = \frac{\partial W}{\partial \mathbf{F}^c} \quad (43)$$

because of

$$\int_{\partial \Omega_0} \mathbf{u}' \otimes \mathcal{N} dS = 0.$$

As the matter of the fact, by the Hill–Mandel condition one can show that

$$\begin{aligned} \mathbf{P}^c : \delta \bar{\mathbf{F}}^c &= \frac{1}{|\Omega_0|} \int_{\Omega_0} \mathbf{P} : \delta \bar{\mathbf{F}} d\Omega = \left(\frac{1}{|\Omega_0|} \int_{\Omega_0} \mathbf{P} d\Omega \right) : \delta \bar{\mathbf{F}}^c + \frac{1}{|\Omega_0|} \int_{\Omega_0} \mathbf{P} : \frac{\partial \delta \mathbf{u}'}{\partial \mathbf{X}} d\Omega \\ &= \bar{\mathbf{P}}^c : \delta \bar{\mathbf{F}}^c + \frac{1}{|\Omega_0|} \int_{\partial \Omega_0} \mathbf{P} \cdot \mathcal{N} \cdot \delta \mathbf{u}' dS - \frac{1}{|\Omega_0|} \int_{\Omega_0} (\nabla_{\mathbf{X}} \cdot \mathbf{P}) \cdot \delta \mathbf{u}' d\Omega \\ &= \bar{\mathbf{P}}^c : \delta \bar{\mathbf{F}}^c + \frac{1}{|\Omega_0|} \int_{\partial \Omega_0} \mathbf{P} \cdot \mathcal{N} \cdot \delta \mathbf{u}' dS. \end{aligned} \quad (44)$$

Since $\mathbf{u}' = 0, \forall \mathbf{X} \in \partial \Omega_0$, we have

$$\bar{\mathbf{P}}^c = \mathbf{P}^c = \frac{\partial W}{\partial \mathbf{F}^c}. \quad (45)$$

This then provides a means and justification to apply the Cauchy–Born rule to the mean field of interfacial interphase zone. That is:

the average lattice vector in a deformed interphase zone may be calculated as follows:

$$\bar{\mathbf{r}}_i = \bar{\mathbf{F}}^c \cdot \mathbf{R}_i, \quad i = 1, 2, \dots, n_c. \quad (46)$$

Subsequently, we can calculate the averaged 1st Piola–Kirchhoff stress tensor in each interphase zone as

$$\bar{\mathbf{P}}^c = \frac{\partial W}{\partial \mathbf{F}^c} = \frac{1}{\Omega_0^c} \sum_{i=1}^{n_c} \frac{\partial \phi_{depl}}{\partial \mathbf{r}_i} \frac{\bar{\mathbf{r}}_i \otimes \mathbf{R}_i}{r_i}. \quad (47)$$

In the proposed AIZM, we are in fact making two coarse graining models: one for the bulk medium and another for the material interphases or defects. Inside the bulk element, there is no fine scale deformation, and the coarse scale deformation is uniform; whereas inside the interphase element deformation at both coarse scale and fine scale is not uniform. After obtaining the stress inside the interphase element, we can readily find cohesive traction along the boundary of interphase zone, which is the same boundary of the adjacent bulk elements with the opposite out normals,

$$\mathbf{T}^{cohe} = \mathbf{P}^c(\bar{\mathbf{F}}^c) \cdot \mathcal{N}, \quad (48)$$

where \mathcal{N} is the out-normal of adjacent bulk FE elements. As shown in Eq. (41), one may express the average deformation gradient as a function of the separation of two FEM boundaries, this implies that

$$\bar{\mathbf{F}}^c = \bar{\mathbf{F}}^c(\Delta) \rightarrow \mathbf{T}^{cohe} = \mathbf{P}^c(\bar{\mathbf{F}}^c(\Delta)) \cdot \mathcal{N}.$$

We have then found the relationships between the cohesive traction and corresponding opening displacements of the interphase zone. In Fig. 12, we plot the both the normal traction–separation and the tangential traction–separation cohesive law with respect to LJ potential.

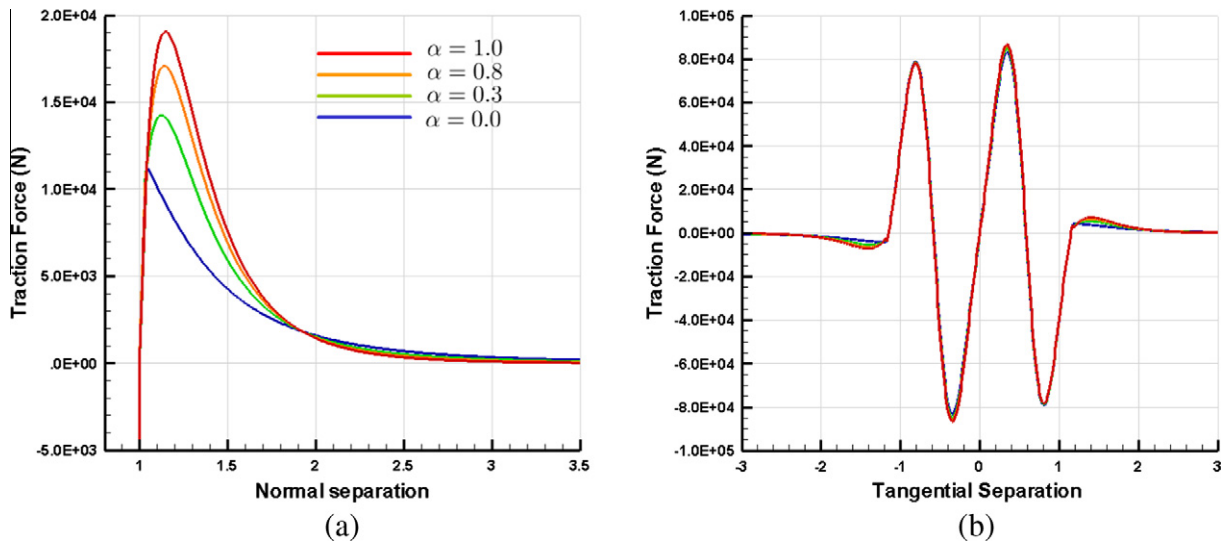


Fig. 12. The cohesive laws of traction and separation: (a) normal traction vs. mode-I surface separation, and (b) tangential traction vs. mode-II surface separation.

Remark 4.1. The above effective deformation gradient and static condensation approach is just an interpretation or an analysis of the proposed AIZM method. However, one can indeed implement AIZM based on this cohesive surface interaction interpretation, which is in fact equivalent to a one-point reduced integration approach on the bulk interphase element. In some cases, we have observe the effect of spurious hour-glass mode along the crack path. In general, the two-point reduced integration algorithm behaves better.

5. Element (mesh) fault energies

In metallic materials, a stacking fault is one or more interruption atomic planes in the stacking sequence of the crystal structure. These interruption planes, or an interruption zone, carry a certain stacking fault energy, γ_s , which is referred to the energy stored between two interrupted layers of a stacking crystal plane sequence. The stacking-fault energy is a material property that can be used to characterize defect evolution such as dislocation motions.

Following a Peierls type of analysis, Rice and coworkers [38–40] have developed a simple criterion for determining the intrinsic ductile versus brittle behavior of materials. Rice proposed that a simple rule to measure the brittle versus ductile behavior of materials is the ratio of two planar fault energies, γ_s/γ_{us} , which determines the competition between dislocation emission from a crack tip and crack cleavage. Dislocation nucleation is characterized by the unstable stacking fault energy γ_{us} , which corresponds to the lowest energy barrier encountered in sliding one half of a crystal relative to another along a slip plane.

In AIZM, one may view the interphase element as an artificial fault between two perfect bulk elements, and it may represent a coarse-grained model for a stack of defect surface layers when the atomistic potential inside the interphase element switching from the bulk potential to the depletion potential.

In the following as an analogous to stacking fault energy, we study the artificial fault energy between two bulk elements. Let the local coordinate X_1 parallel to the element mesh boundary considered. Hence we may denote \bar{u} as the relative effective horizontal (tangential) opening displacement, and \bar{v} as the relative effective vertical (normal) opening displacement of the interphase zone. Therefore, one may find that the traction along the element boundary is an explicit function of the effective deformation gradient inside the interphase zone. For LJ-potential, the effective deformation gradient inside the interphase element for the cases of pure Mode-I and pure Mode-II are given separately as follows,

$$\bar{\mathbf{F}}_n = \begin{bmatrix} 1, & 0 & 0 \\ 0, & 1 + \bar{v}/R_0 & 0 \\ 0, & 0, & 1 \end{bmatrix} \text{ and } \bar{\mathbf{F}}_t = \begin{bmatrix} 1, & \bar{u}/R_0, & 0 \\ 0, & 1, & 0 \\ 0, & 0, & 1 \end{bmatrix}, \quad (49)$$

where R_0 is the thickness of the interphase element. Substituting the relations in Eq. (49) into (48), one can find the relationship between the element traction and the relative separation (opening displacements) of the interphase zone.

In Fig. 12, the cohesive relations of both normal traction/normal opening displacement (Mode-I) and tangential traction/shear opening displacement (Mode-II) are displayed, which are calculated based on Eqs. (48) and (49).

A major advantage of AIZM is that it can easily provide cohesive traction along the bulk element boundary for both normal and tangential traction from a same expression Eq. (48), whereas in conventional cohesive FEM approach, these two traction are given separately, and they are not related to lattice structure or atomistic potential.

In general, the longitudinal direction of the soft interphase zone may be viewed as a fault, or more precisely an element (mesh) fault, because we assume that total deformation field at macroscale is piece-wise constant. In this context, this kinematic assumption is not just a convenience for finite element discretization, but a physical modeling to mimic the defect distribution, which is very similar to the kinematics of crystal plasticity, e.g. [44]. The ability to evaluate the element fault energy will help us design multiscale simulations that have predictive power. In this section, we shall focus on analysis and calculation element fault energies.

From materials science perspective, the fault energy should be determined by bulk material properties, such as fault formation, orientation, as well as configuration. The mesh fault energy discussed in this paper is subjected to additional constraints because of chosen finite element discretization. In the AIZM model, these factors are reflected by the depletion potential, mesh orientation, lattice orientations in both bulk element as well as in the interphase element. As a matter of fact, the phenomenological cohesive tangential law proposed by Xu and Needleman [49] is in a way of mimicking the shape of stacking fault energy (see also [13]). In general, the tangential interfacial cohesive potential should be related to stacking fault energy, or antiphase boundary energy, or other interfacial cohesive potential energies, all of which are physical quantities that may be directly calculated by using first principle based methods. Therefore, it makes sense only if we can successfully build an AIZM model to relate the mesoscale interface potential to microscale atomistic potential.

Indeed, both the lattice orientation in the interphase zone and the FE mesh are very important factors in the element fault energy calculations. In this first study, we shall examine some simple cases under plane strain condition. Consider that the crystalline solid is a single crystal that has hexagonal symmetry. Hence the lattice orientation in each bulk element will be the same. Let the finite element mesh boundary coincides with the possible slip line direc-

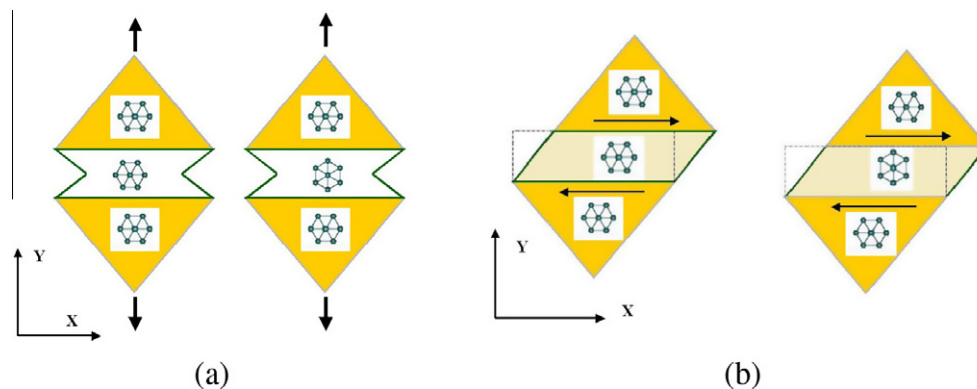


Fig. 13. Interphase zones under normal and tangential traction.

tions, so that in the slip line strip the original lattice may be rotated, distorted, or remaining the same. In the case discussed in this paper we assume that the symmetry inside the interphase zone remains hexagonal, but it may be rigidly rotated to a fixed angle. We consider two cases: (I) one pair of the hexagonal axes are parallel to the element boundary, and (II) one pair of the hexagonal axes are perpendicular to the element boundaries. We now calcu-

late the interphase zone potential energies, or the mesh stacking fault energies, in terms of both interface normal opening (model-I) and the tangential opening (model-II).

Since the deformation gradient is only the function of interface opening displacement, the bulk atomistic potential may directly be linked to the coarse-grain traction/displacement potential, and this is how:

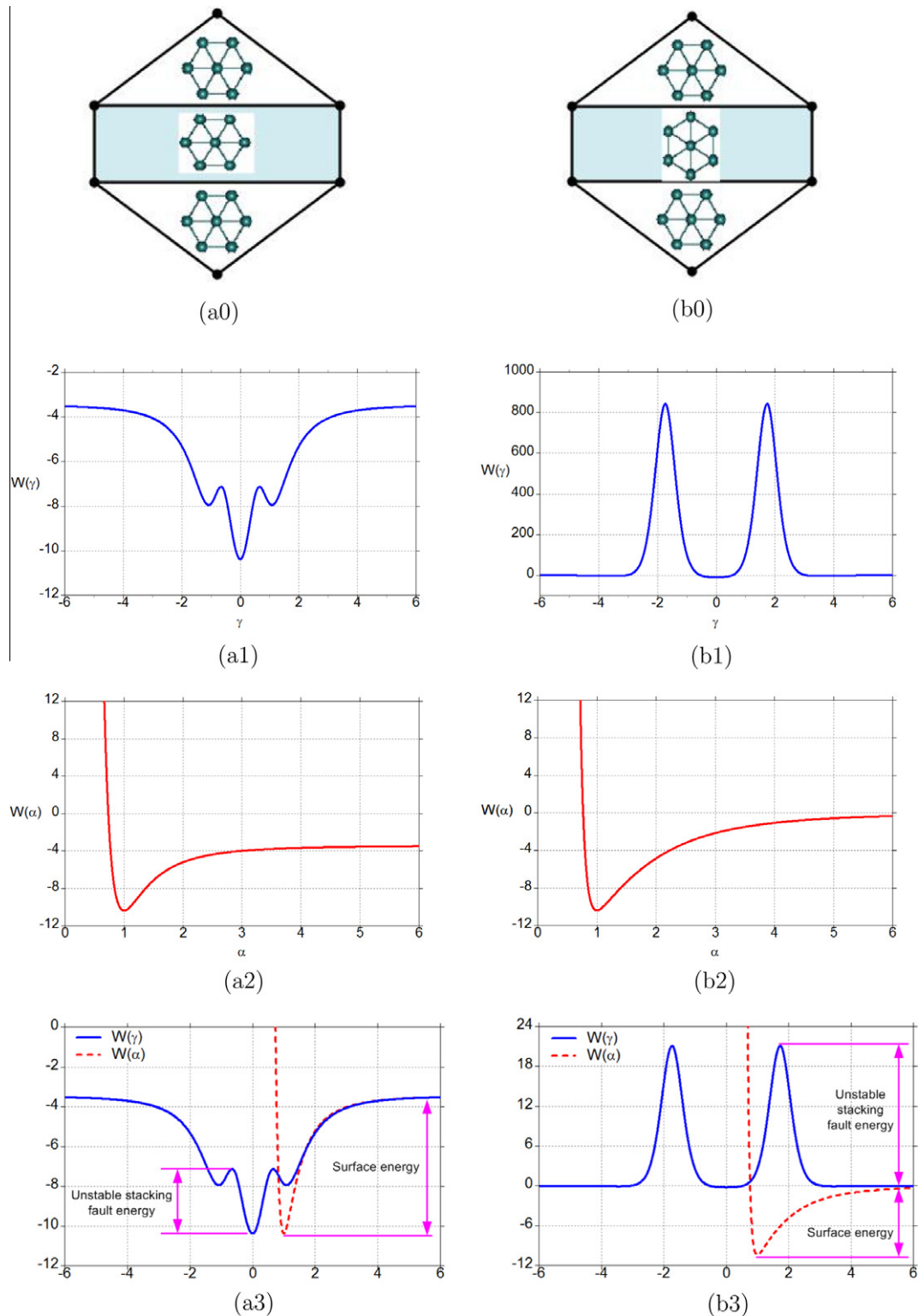


Fig. 14. Comparison of surface energy and stacking fault energy with respect to different mesh fault orientations: (a1)–(b1) unstable stacking fault energy, (a2)–(b2) cohesive surface energy, and (a3)–(b3) γ_{us} vs. $2\gamma_s$ inside the interphase element: solid line–stacking fault energies, dash line–surface energies.

$$W_n(\bar{v}) = \beta_c \sum_{i=1}^6 \phi_{\text{depl}}(r_i(\bar{v})), \quad \text{and} \quad W_t(\bar{u}) = \beta_c \sum_{i=1}^6 \phi_{\text{depl}}(r_i(\bar{u})), \quad (50)$$

in which $\mathbf{r}_i = \bar{\mathbf{F}}_n(\bar{v}) \cdot \mathbf{R}_i$ or $\mathbf{r}_i = \bar{\mathbf{F}}_t(\bar{u}) \cdot \mathbf{R}_i$, and β_c is the atom density in the interphase zone.

Substituting Eq. (49) into (50) and considering the relative interphase zone opening displacements as the effective displacements inside the interphase zone, we can find the surface energy and stacking fault energy in terms of the effective displacements. However, the calculation of element fault energy depends on the lattice structure inside the interphase zone. Here we are considering two cases of different lattice orientations of hexagonal lattices: For Case I,

$$\mathbf{R}_i = a \left\{ \cos\left(\frac{(i-1)\pi}{3}\right), \sin\left(\frac{(i-1)\pi}{3}\right) \right\}, \quad i = 1, 2, \dots, 6 \quad (51)$$

and for Case II

$$\mathbf{R}_i = a \left\{ \cos\left(\frac{\pi}{6} + \frac{(i-1)\pi}{3}\right), \sin\left(\frac{\pi}{6} + \frac{(i-1)\pi}{3}\right) \right\}, \quad i = 1, 2, \dots, 6. \quad (52)$$

Two interphase zone element benchmark tests have been conducted, which are illustrated in Fig. 13, and the corresponding element or mesh stacking fault energies are depicted in Fig. 14. One may find that in Case I, the unstable stacking fault energy ($\gamma_{us} = 3.25$) is smaller than the corresponding surface energy ($2\gamma_s = 6.85$), the ratio between the two is

$$\alpha_I = \frac{\gamma_{us}}{2\gamma_s} = 0.47 < 1, \quad (53)$$

whereas in the second case, the unstable stacking fault energy ($\gamma_{us} = 843.27$), which is much larger (in Fig. 14 we scale the original value by a factor of 40 for better visualization purpose) than that of the cohesive surface energy ($2\gamma_s = 10.02$), the ratio between the two is

$$\alpha_{II} = \frac{\gamma_{us}}{2\gamma_s} = 84.16 \gg 1. \quad (54)$$

Based on this analysis, we may expect the ductile fracture for Case I, because the unstable stacking fault energy is smaller than the surface energy, and the lattice sliding is more susceptible than the lattice cleavage opening along the allowable kinematic failure mode—that is element boundary; whereas in Case II the peak value of unstable stacking energy is about 84 times larger than that of the surface energy, the lattice is more susceptible to cleavage opening than sliding along the allowable element boundary.

Therefore we would expect brittle fracture for Case II. In the next section, we shall use the both lattice orientations and corresponding mesh fault set-up to simulate crack propagations, compare the results between them, and verify the above analytical predictions.

In fact, one may also consider applying AIZM to polycrystalline solids. In the case of polycrystal solids, the lattice orientation inside the interphase zone may be affected by the adjacent single crystal elements in both sides, which may have different lattice orientations. An in-depth study on applying AIZM to polycrystal solids can be found in [33]. Above analysis has shown that the element stacking fault energies not only depend on the bulk lattice orientation, but also depend on the microstructure of the interphase. The above example has demonstrated two points: first it is shown that by altering the interphase microstructure one may be able to use AIZM to simulate a specific stacking fault energy (SFE) of a given material; and second it may also hint the fact that the interphase energy is strongly dependent on interphase microstructure. Be more specific, we have basically shown that the interphase energy is a functional of orientational quantity with a tensorial field, which may play significant role in material failure as shall be discussed in next section.

We note in passing that (1) all interphase elements constructed can be made as part of the lattice slip planes or grain boundaries, i.e. orientation of all interphase zones can be chosen along certain atomic planes, so they are physical entities; and (2) even though most of the calculations shown in this paper are based on pair potential, the underline principle can be applied for any other atomistic potentials of different atomistic bonds, for example the EAM potential for metallic bonding.

Similarly, the effective deformation gradient in each interphase element can be also updated. For the case of plane strain, it is updated based on the following equations,

$$\begin{bmatrix} \bar{F}_{11}^c(t_n) \\ \bar{F}_{12}^c(t_n) \\ \bar{F}_{21}^c(t_n) \\ \bar{F}_{22}^c(t_n) \end{bmatrix} = \begin{bmatrix} 1 \\ 0 \\ 0 \\ 1 \end{bmatrix} + \frac{1}{2LR_0} \begin{bmatrix} d & 0 & -b & 0 \\ -c & 0 & a & 0 \\ 0 & d & 0 & -b \\ 0 & -c & 0 & a \end{bmatrix} \begin{bmatrix} u_{I+1}^+(t_n) - u_I^-(t_n) \\ v_{I+1}^+(t_n) - v_I^-(t_n) \\ u_I^+(t_n) - u_{I+1}^-(t_n) \\ v_I^+(t_n) - v_{I+1}^-(t_n) \end{bmatrix}, \quad (55)$$

where $(u_I^\pm(t_n), v_I^\pm(t_n)) = \mathbf{d}_I^\pm(t_n)$, and the meaning of the superscripts \pm is referred to Fig. 11 for their definitions; L is side length of the adjacent bulk elements, and R_0 is the thickness of the interphase element. The constants, a, b, c, d , are defined in Eq. (41). The stress inside the interphase zone can then be updated by using Eq. (47).

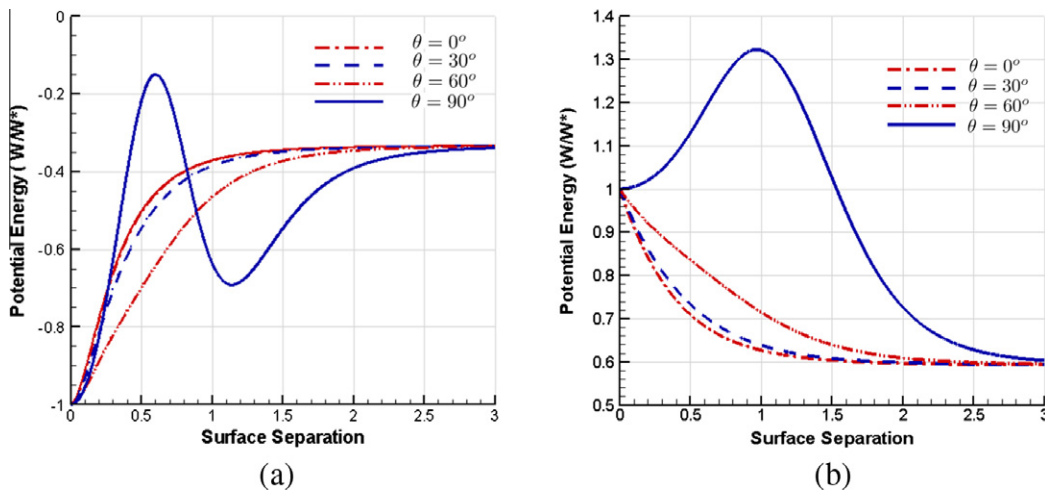


Fig. 15. Mixed-mode interphase potential: (a) based the Lennard-Jones potential, and (b) based on the embedded atom method (EAM) potential.

5.1. Mixed-mode interface potential

One of advantages of AIZM over conventional CZM is that it furnishes a coarse-grained mixed interface potential automatically. Let

$$W = \frac{1}{\Omega_0} \sum_{i=1}^n \phi_{intp}(r_i), \quad \mathbf{r}_i = \bar{\mathbf{F}}_c(\Delta) \cdot \mathbf{R}_i.$$

Consider a mixed mode displacement load sequence parameterized by a loading angle θ , which is the angle between the load displacement direction and the normal direction of the interface. The load sequence can be represented by the effective deformation gradient inside the interphase element, which is related to the interface displacement separation vector (\bar{u}, \bar{v}) . For a plane strain problem, it may be written as follows,

$$[\bar{\mathbf{F}}_{ii}] = \begin{bmatrix} 1 & \bar{u}/R_0 & 0 \\ 0 & 1 + \bar{v}/R_0 & 0 \\ 0 & 0 & 1 \end{bmatrix}, \quad \bar{u} = D_0 \sin \theta, \quad \bar{v} = D_0 \cos \theta.$$

In the following figure, we plot the interface traction-separation potential versus the surface separation, D_0 . The above mixed-mode cohesive interface potential is plotted by using the interface atomistic potential ϕ_{intp} , ($\alpha = 1$). In Fig. 15, the interface cohesive potential is plotted with respect to $\theta = 0, \pi/6, \pi/3$, and $\pi/2$. In the case (a), the Lennard-Jones potential is used in the calculation, and in case (b) the Sutton–Chen potential—an embedded atom potential is used in the calculation of interface cohesive traction/separation potential. The exact expression of the EAM potential will be given in Section 6.

One may observe a mixed-mode transition of interface cohesive potential and its dependence on loading angle θ . This shows advantages over the ad hoc mixed mode cohesive zone models, e.g. [36].

6. Simulation examples

In this section, we present six numerical examples that have been carried out by using the proposed atomistic-based interphase zone finite element method.

6.1. Example I: validation of AIZM method by MD simulations

To validate the proposed AIZM method, we have applied it to simulate a special dynamic fracture problem that has been thoroughly studied in the literature [7,48]. The computation results of AIZM method are compared with that of the MD simulation conducted by Buehler et al. [7]. The exact problem statement is shown in Fig. 16, in which a 2D plate with dimension ($L_x \times L_y = 8625 \times 3450$ with $L_x/L_y = 2.5$) is under dynamically prescribed uniaxial tension load. There is a pre-crack at the left side of the plate, and the pre-crack tip is located at ($L_c = L_x/5 = 1725$). Under the dynamic loading, the crack propagates along the horizontal direction (the x direction) in the middle of the plate. For the purpose of comparison, all quantities in these simulations are in reduced units. The specimen size in reduced units is about micrometer in physical dimensions. The interfacial lattice is the hexagonal lattice with the equilibrium bond distance $r_1 = 2^{1/6}$, and the crystal orientation is shown in Fig. 16 (a). The lattice orientation inside the interphase zone is chosen the same as that of the bulk elements. To avoid crack branching, a weak fracture layer is introduced (see Fig. 16(a)) by assuming that the cohesive strength in the rest of the slab are much stronger than the cohesive strength in the weak layer. We use exactly the same biharmonic interatomic potential used by Buehler et al. [7], which is composed of two spring constants $k_1 = 36/2^{1/3} \approx 28.57$ and $k_2 = 2k_1$, and it is linearized from the Lennard-Jones (LJ) potential (see Eq. (29)):

$$\phi(r) = \begin{cases} \frac{1}{2}k_1(r - r_1)^2, & \text{if } r < r_{on}, \\ a_2 + \frac{1}{2}k_2(r - r_2)^2, & \text{if } r \geq r_{on}, \end{cases} \quad (56)$$

where $a_2 = \frac{1}{2}k_1(r_{on} - r_1)^2 - \frac{1}{2}k_2(r_{on} - r_2)^2$ and $r_2 = \frac{1}{2}(r_{on} + r_1)$ with $r_{on} = r_1(1 + \epsilon_{on})$. The parameter r_{on} governs the onset strain (ϵ_{on}) of the hyperelastic effects.

All the material constants are chosen exactly the same as in Buehler et al.’s simulations. In the simulation reported in this paper, there are 16,000 bulk elements used with the characteristic dimension of 20–30 nm, and there are 23,860 interphase elements used with the thickness of five atomic spacings. In the original MD computation carried out by Buehler et al. [7], there are more than 50 million atoms in the simulation.

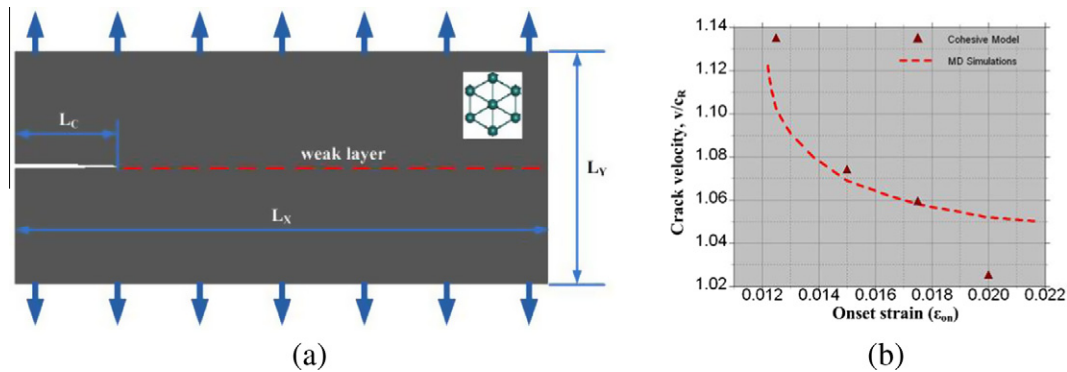


Fig. 16. (a) The simulation geometry with lattice orientation and the weak layer, and (b) comparison of crack speeds.

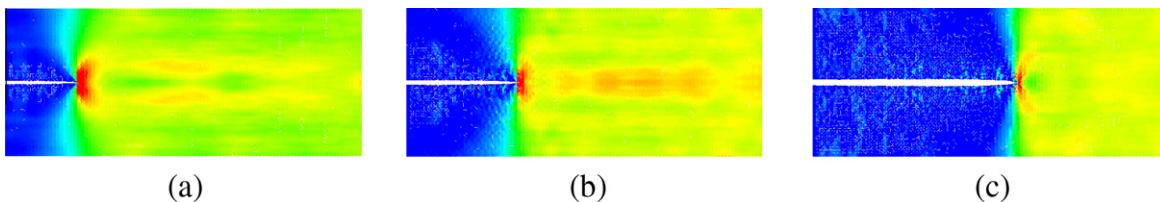


Fig. 17. Time sequence of crack propagation.

Constant strain rate ($\dot{\epsilon} = 1.16 \times 10^{-5}$) is applied over the loading period to strain the system. A time sequence of the crack propagation process along the weak layer is shown in Fig. 17. We compute the crack propagation speeds by using AIZM method with different onset strains, and then we compare our numerical results with the crack speeds obtained from the MD simulations using the same potential and the same material constants [7]. The comparison between the results of AIZM method and that of the MD simulation is shown in Fig. 16(b). In Fig. 16(b), one may find that for intermediate value of the onset strains the results obtained by using AIZM method agrees well with the results obtained by using molecular dynamics.

6.2. Example II: ductile fracture vs. brittle fracture

In this example, we apply AIZM model to simulate crack propagations at macroscale. We assume that the testing material is a single crystal with hexagonal symmetry. In the simulations, all triangle elements are chosen as equilateral triangles that align

their boundary along the directions of the hexagonal lattice in the bulk element. In interphase elements, we choose two sets of hexagonal lattices: (1) the one with the same orientation as in the bulk element, and (2) the hexagonal lattice that rotates an angle of $\pi/6$ with respect to the lattice orientation in the bulk element. The two lattice structures are shown in Fig. 18 (a) and (b). The LJ potential is used in bulk elements, and the depletion potential in Eq. (30) is used as the atomistic potential inside the interphase zone. We set $\epsilon = 1$ and $\sigma = 1$ for the bulk and interphase atomistic potentials (see Eqs. (29) and (30)).

In the simulation, the test specimen is a 2D plate with dimension (2 mm \times 2 mm) that is subjected to unilateral tension in Y-axis (see Fig. 18), there is a pre-crack at the left side of the plate. There are total 9520 interphase elements and 6400 triangular bulk elements. The time step is chosen as $\Delta t = 1 \times 10^{-10}$ s. The process of the crack growth is displayed in Figs. 18(a1)–(a7) and 18(b1)–(b7) for both cases. The mesh stacking fault energies for both cases have been calculated in the previous section. Since in Case I, the unstable element fault energy is smaller than the element surface energy, it

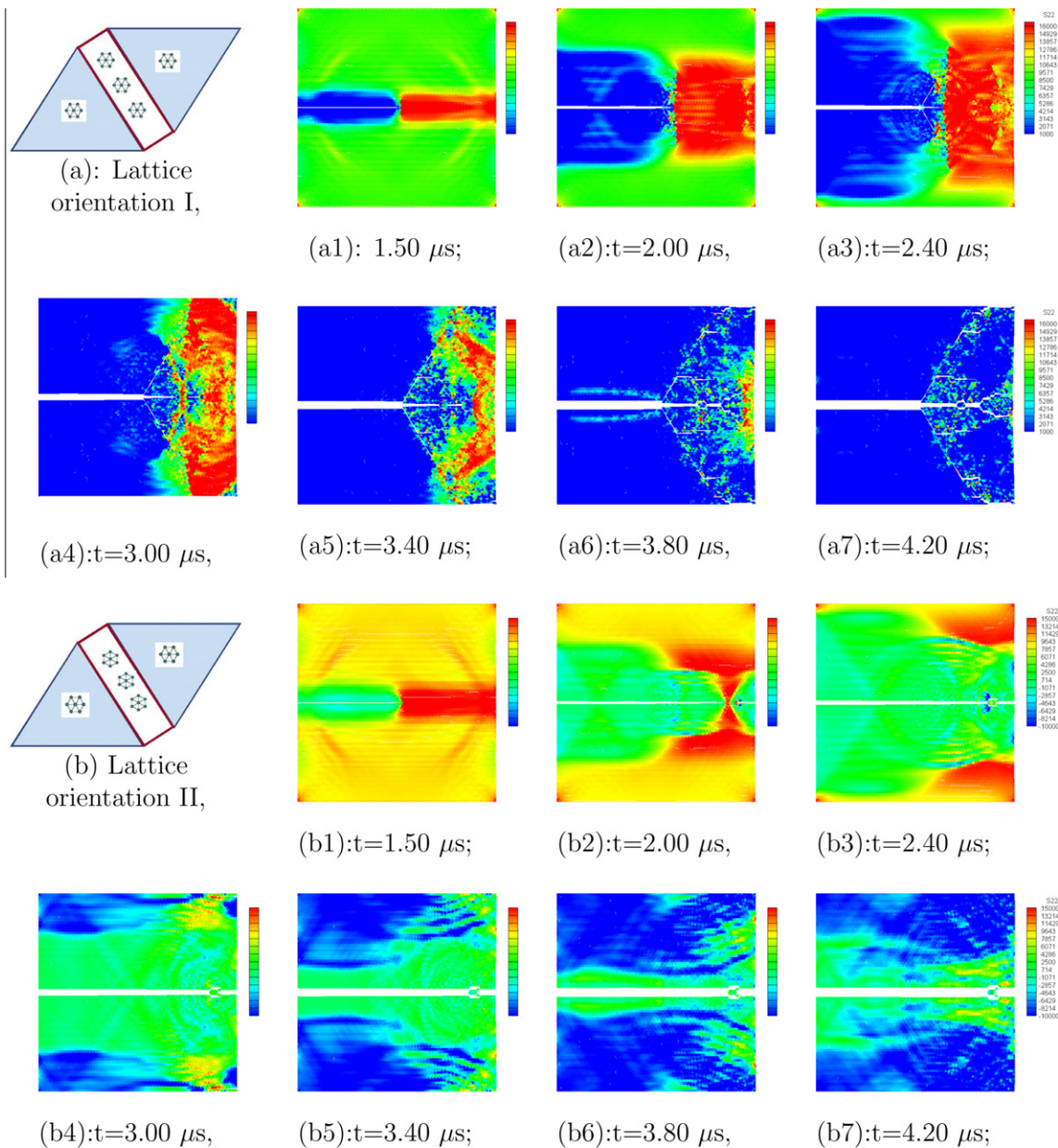


Fig. 18. Stress distribution for crack propagations vs. different interphase lattice orientations.

exhibits a typical ductile fracture pattern so that the crack path is almost along the direction of element boundary where the shear stress is maximum. Whereas in Case II, the mesh stacking fault energy is much larger than the cohesive surface energy, it exhibits the typical brittle failure pattern with the crack grows along the horizontal line that is aligned with the initial pre-notch direction, or the crack direction is along with the element boundary where the normal stress is maximum. However, void formation at the crack tip can also be observed in some simulations with different parameters, which may need in-depth study.

6.3. Example III: simulations of high-speed impact and spall fracture

To illustrate the versatility of AIZM, we have carried out numerical computations to simulate high-speed impact induced spall fractures, which is a very difficult problem that has been elusive to many existing numerical methods [1]. The simulation problem is a rigid projectile impacting a deformable plate. The projectile is a (1.02 mm × 0.09 mm) rigid block with impact velocity $v = 100$ m/s, the target is a (1 mm × 0.4 mm) block with free boundary. In this simulation, there are totally 23,860 interphase elements and 16,000 triangular bulk elements in the target. The atomistic potentials and lattice orientations for both the bulk element as well as the interphase element are exactly the same as in Example III (a).

In this example, the time step is chosen as $\Delta t = 1 \times 10^{-10}$ s. Contact problems are characterized by impenetrability conditions that needs to be enforced during computation. We adopted the exact enforcement of the impenetrability condition in a single time step (see [18]). The simulation results are shown in Fig. 19. The

wave propagation from the contact point to the opposite boundary has been observed. The phenomenon of spall fracture under impacts has been captured (see Fig. 19).

6.4. Example IV: fracture in poly-crystalline material

In this example, we apply AIZM method to simulate fracture in polycrystalline solids. We consider a (1 mm × 1 mm) polycrystalline block that is subjected to unilateral tension as shown in Fig. 20. There are 121 grains and 2376 bulk elements in the model. A horizontal pre-crack is set boarding with several grain boundaries.

In AIZM calculation, each grain is randomly assigned a lattice orientation. The lattice orientation along grain boundaries may be assigned according to various considerations and assumptions. For simplicity and demonstration purpose, the lattice orientation in each grain boundary, β is taken as the average of orientations of the two adjacent grains α_1, α_2 , i.e.

$$\beta = \frac{1}{2}(\alpha_1 + \alpha_2) \quad (57)$$

as shown in Fig. 21. For the first case, in both the grain and the grain boundary the depletion potentials of the interphase zone have same energy depth, i.e.,

$$\epsilon_{depl}^i = \epsilon_{depl}^b \quad (58)$$

From Fig. 22(a), it can be seen that crack propagation can go through grains. However, if the cohesive strength in interphase elements inside a grain is set to be much stronger than that of the grain boundary, e.g.

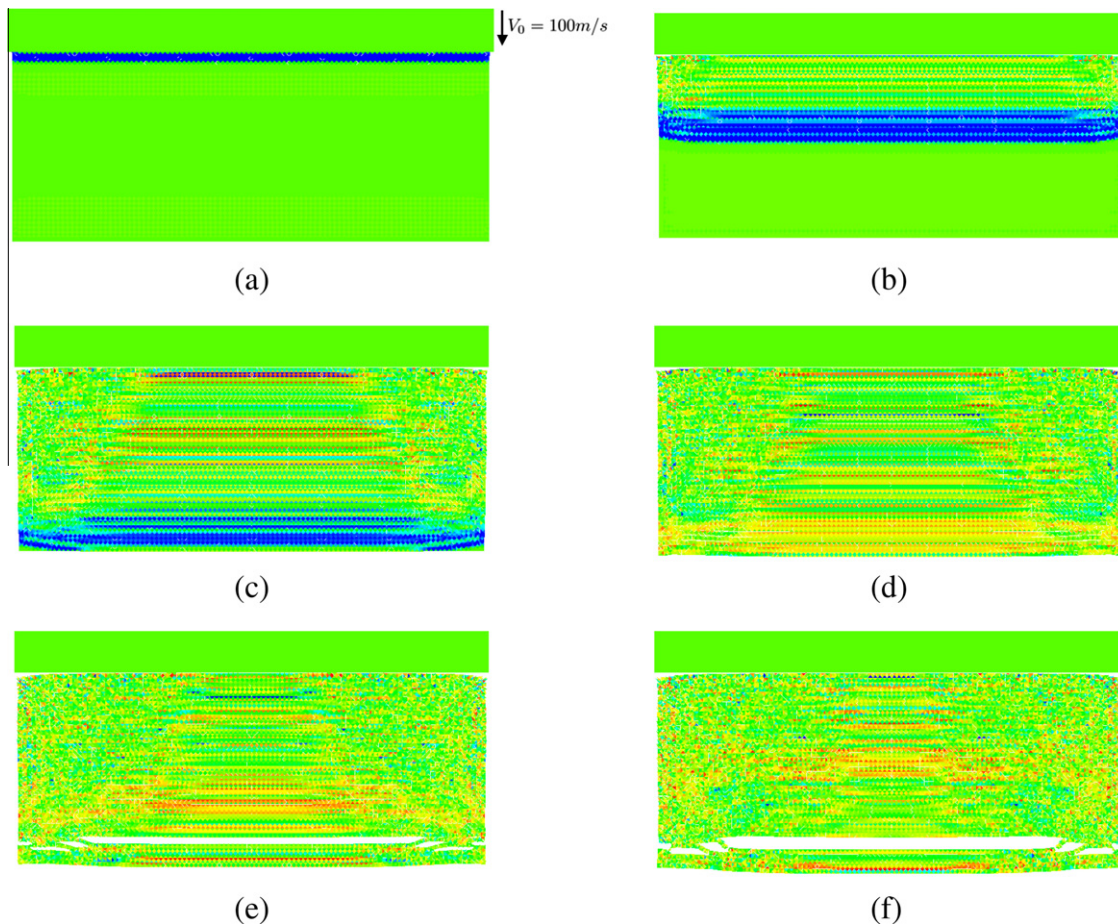


Fig. 19. The snapshot of stress distribution of a spall fracture due to impact: (a) $t = 0.15 \mu\text{s}$; (b) $t = 0.35 \mu\text{s}$; (c) $t = 0.6 \mu\text{s}$; (d) $t = 0.7 \mu\text{s}$; (e) $t = 0.85 \mu\text{s}$; and (f) $t = 1.0 \mu\text{s}$.

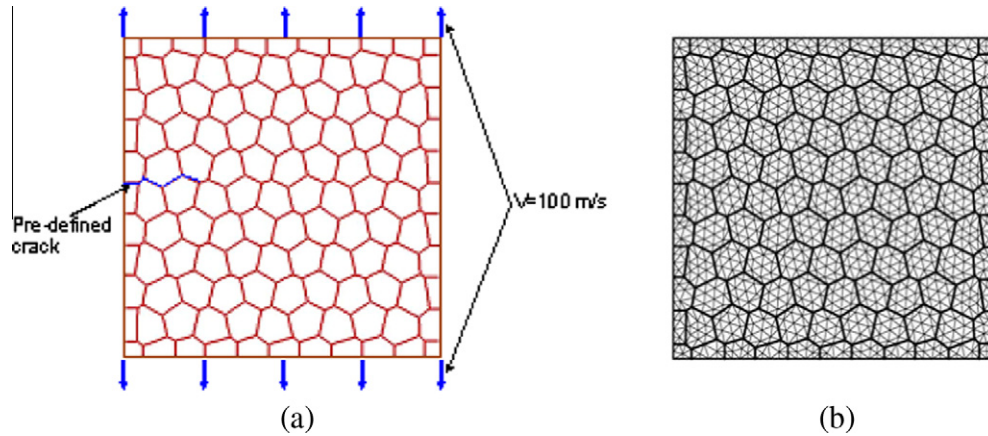


Fig. 20. A polycrystal plate with a notch under dynamic loading.

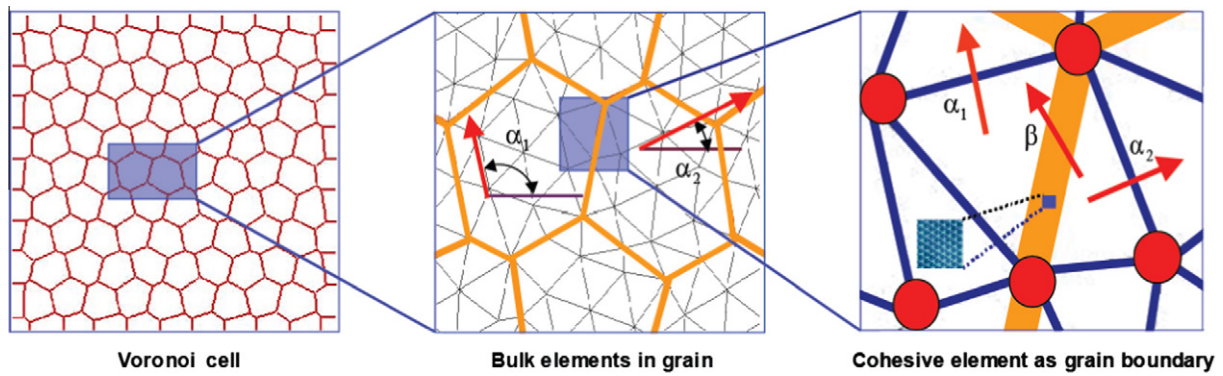


Fig. 21. How to determine crystal orientation inside the grain boundary.

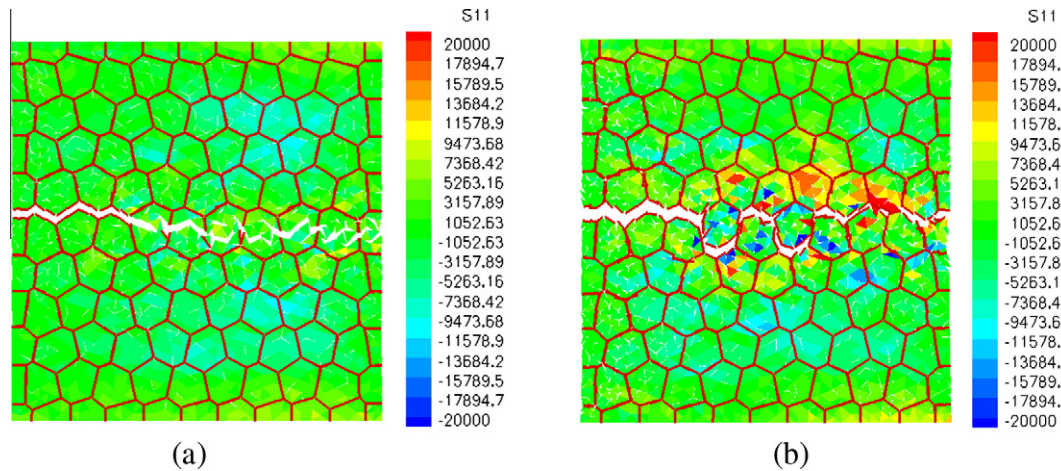


Fig. 22. The snapshot of stress distribution of fractures in a polycrystalline solid: (a) transgranular fracture, and (b) intergranular fracture.

$$\epsilon_{depl}^i = 5\epsilon_{depl}^b \tag{59}$$

The crack path will only follow grain boundaries as in Fig. 22(b). The computation details of this example can be found in [33]. In this example, the LJ-potential is used in bulk element, and the corresponding depletion potential (30) is used in the interphase element.

6.5. Example V: three-dimensional fracture

One of the strengths of the atomistic-based interphase zone model is its computational flexibility and robustness in three-

dimensional simulation of fractures, which has been a challenge for many other numerical methods.

Here we first present an illustrative example of AIZM simulation of three-dimensional crack propagation. The example considered is a single crystal specimen with FCC structure. Since the deformation in the bulk element is assumed to be uniform, we use the tetrahedron element for bulk elements, and we use a six-node wedge element for interphase elements as shown in Fig. 23(a) and (b). Similar to two-dimensional cases, each interphase element is sandwiched by two bulk elements. The main technical gradients of 3D calculations remain the same as that of

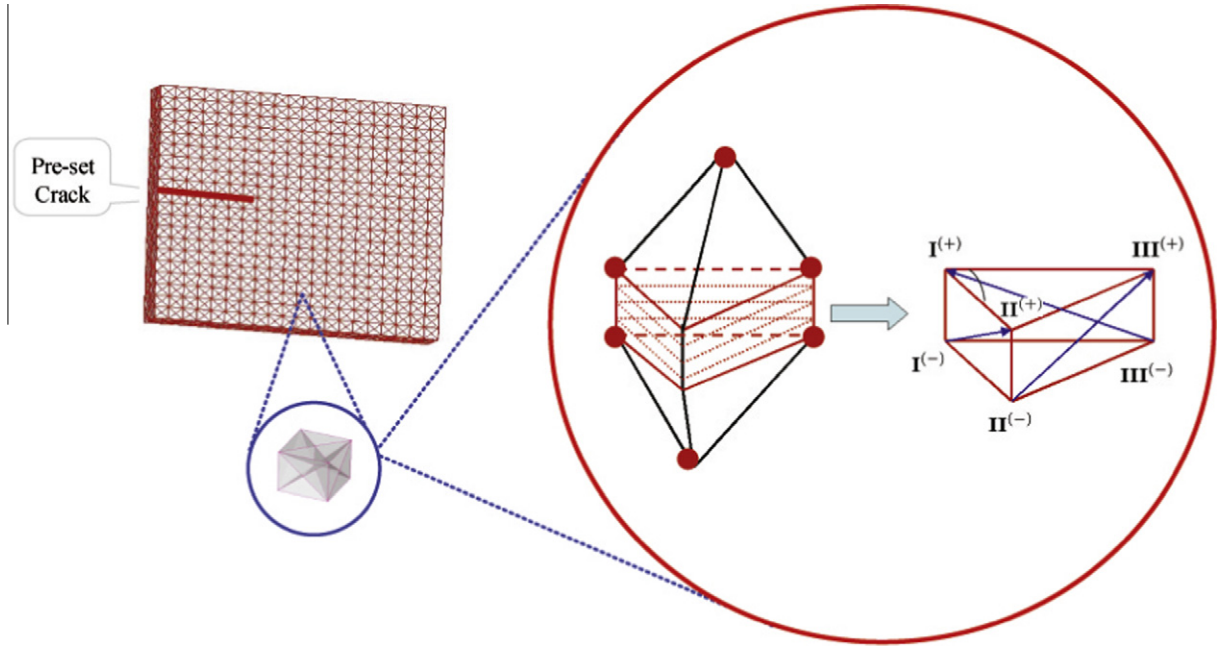


Fig. 23. Three-dimensional AIZM model: bulk element + interphase element, and interphase element nodal numbering.

2D calculations, except that the reduced integration technique and how to evaluate average deformation gradient inside the interphase zone are different from 2D cases. The reduced integration of 3D wedge shape interphase element has been demonstrated in Fig. 10.

In the following, we briefly outline an equivalent cohesive zone approach, which is also equivalent to a one-point integration approach.

We first determine the average deformation gradient in the interphase element. To do so, one may choose an arbitrary set of three non-planar lines across the interphase zone to find the effective deformation gradient.

Based on the choice of Fig. 23 (b), we can define the following vectors,

$$\Delta \mathbf{x}_i = \begin{bmatrix} x_{III}^+ - x_{II}^- \\ x_{IV}^+ - x_{III}^- \\ x_{II}^+ - x_{III}^- \end{bmatrix} \quad \text{and} \quad \bar{\mathbf{F}}_i = \begin{bmatrix} \bar{F}_{i1} \\ \bar{F}_{i2} \\ \bar{F}_{i3} \end{bmatrix}, \quad i = 1, 2, 3. \quad (60)$$

where $\Delta \mathbf{x}_i$, $i = 1, 2, 3$ are position vectors of three non-planar line segments chosen to determine effective deformation gradient $\bar{\mathbf{F}}$, and $\bar{\mathbf{F}}_i$, $i = 1, 2, 3$ are just the row vector of effective deformation gradient inside the interphase zone. By the Hill–Mandel lemma, it is not difficult to see that \mathbf{x}_i and $\bar{\mathbf{F}}_i$ are related by the following relation,

$$\mathbf{x}_i = \bar{\mathbf{F}} \cdot \mathbf{X}_i, \quad i = 1, 2, 3,$$

where \mathbf{X}_i are un-deformed line segments in the referential configuration. Hence, we can derive the following algebraic equations

$$\begin{bmatrix} \Delta \mathbf{x}_1 \\ \Delta \mathbf{x}_2 \\ \Delta \mathbf{x}_3 \end{bmatrix} = \begin{bmatrix} [\Delta \mathbf{X}] & 0 & 0 \\ 0 & [\Delta \mathbf{X}] & 0 \\ 0 & 0 & [\Delta \mathbf{X}] \end{bmatrix} \begin{bmatrix} \bar{\mathbf{F}}_1 \\ \bar{\mathbf{F}}_2 \\ \bar{\mathbf{F}}_3 \end{bmatrix}, \quad (61)$$

where the matrix $[\Delta \mathbf{X}]$ is defined as

$$[\Delta \mathbf{X}] = \begin{bmatrix} X_{III1}^+ - X_{II1}^-, & X_{III2}^+ - X_{II2}^-, & X_{III3}^+ - X_{II3}^- \\ X_{IV1}^+ - X_{III1}^-, & X_{IV2}^+ - X_{III2}^-, & X_{IV3}^+ - X_{III3}^- \\ X_{II1}^+ - X_{III1}^-, & X_{II2}^+ - X_{III2}^-, & X_{II3}^+ - X_{III3}^- \end{bmatrix}.$$

In fact, Eq. (61) is equivalent to the following three sets of equations,

$$[\Delta \mathbf{x}_i] = [\Delta \mathbf{X}] [\bar{\mathbf{F}}_i], \quad i = 1, 2, 3,$$

which are easy to solve in computations. One can see from Fig. 24(b) that there are twelve nearest neighbor atoms in a FCC Wigner–Seitz cell,

$$\begin{aligned} \mathbf{R}_1 &= a(\cos(\pi/4), 0, \sin(\pi/4)), \\ \mathbf{R}_2 &= a(-\cos(\pi/4), 0, \sin(\pi/4)), \\ \mathbf{R}_3 &= a(-\cos(\pi/4), 0, -\sin(\pi/4)), \\ \mathbf{R}_4 &= a(\cos(\pi/4), 0, -\sin(\pi/4)), \\ \mathbf{R}_5 &= a(\cos(\pi/4), \sin(\pi/4), 0), \\ \mathbf{R}_6 &= a(-\cos(\pi/4), \sin(\pi/4), 0), \\ \mathbf{R}_7 &= a(-\cos(\pi/4), -\sin(\pi/4), 0), \\ \mathbf{R}_8 &= a(0, \cos(\pi/4), -\sin(\pi/4)), \\ \mathbf{R}_9 &= a(0, \cos(\pi/4), \sin(\pi/4)), \\ \mathbf{R}_{10} &= a(0, -\cos(\pi/4), \sin(\pi/4)), \\ \mathbf{R}_{11} &= a(0, -\cos(\pi/4), -\sin(\pi/4)), \\ \mathbf{R}_{12} &= a(0, \cos(\pi/4), -\sin(\pi/4)). \end{aligned}$$

Hence, the effective stress inside an interphase element may be calculated as

$$\bar{\mathbf{P}} = \frac{\partial W}{\partial \bar{\mathbf{F}}^c} = \frac{1}{\Omega_0^c} \sum_{i=1}^{12} \frac{\partial \phi_{intp}}{\partial \bar{r}_i} \frac{\bar{\mathbf{r}}_i \otimes \mathbf{R}_i}{\bar{r}_i}. \quad (62)$$

We have conducted a numerical experiment on ductile fracture, in which a thin plate with notch is subjected to uniaxial tension. The lattice structures in both the bulk element and the interphase zone are FCC lattice. The pre-notched plate is shown in Fig. 24. The plate is 1 mm × 1 mm in size. There are total of 2400 bulk tetrahedron elements and 4300 interphase wedge elements used in computation. The standard Lennard-Jones potential is used in the bulk element, and the depletion potential in Eq. (30) is used as the interphase potential inside the interphase zone. A prescribed displacement (velocity) boundary condition is imposed at the both lateral sides of the plate. A time sequence of fracture is displayed in Fig. 25. From Fig. 25, clearly one may find the ductile fracture patterns with three-dimensional features, such as crack bifurcation along {111} and {110} planes. In three-dimensional calculation,

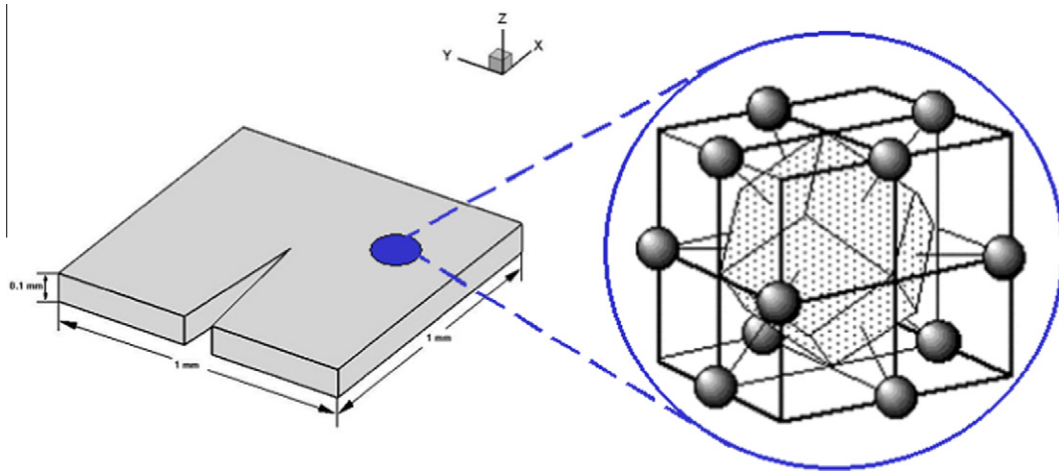


Fig. 24. A three-dimensional pre-notched plate with FCC crystals.

for the purpose of illustration, we again used the LJ-potential in bulk elements, and the depletion potential (30) is used inside the interphase zone. In the following example, we show how to use the embedded atom method in a three-dimensional AIZM calculation.

6.6. Example VI: simulation of projectile fragmentation via AIZM

In this example, we simulate the fragment of a projectile made by aluminum alloy power during high speed impact and penetration of thin aluminum plate.

We choose the multi-body Sutton–Chen (SC) potential [32] as the bulk material's atomistic potential, which is a special embedded atom method (EAM) potential designed for aluminum metals. For an chosen atom i in the bulk element,

$$\phi_{\text{bulk}}(r) = \epsilon \left\{ \frac{1}{2} \sum_{j \neq i} \left(\frac{a}{r_{ij}} \right)^n - c \sqrt{\rho_i} \right\}, \quad (63)$$

where ρ_i is the electron density at the site of atom i ,

$$\rho_i(r) = \sum_{i \neq j} \left(\frac{a}{r_{ij}} \right)^m$$

and ϵ , c , a , m , n are material constants obtained by fitting the atomistic potential (Eq. (63)) with the results obtained from ab initio calculation based on a stable bulk configuration. In EAM potential there are two distinct contributions: the pair potential part and embedding electron density part.

Inside interphase elements, we use the general interphase potential expression,

$$\phi_{\text{intp}}(r) = \alpha \phi_{\text{bulk}}(r) + (1 - \alpha) \phi_{\text{depl}}(r). \quad (64)$$

However, in our approach, the depletion potential is chosen as the coarse-grain potential of the pair potential part in the EAM potential, i.e.

$$\phi_{\text{depl}}(r) = \frac{\epsilon}{2\Omega_0^u} \sum_{j \neq i} \int_{\text{half-space}} \left(\frac{a}{\ell} \right)^n dV, \quad \text{with } dV = \pi \ell r^2 dz, \\ \ell = \sqrt{r^2 + (z - r_{ij})^2} = \frac{\epsilon \pi a^3}{\Omega_0^u (n-2)(n-3)} \sum_{j \neq i} \left(\frac{a}{r_{ij}} \right)^{n-3}. \quad (65)$$

The parameter for the Sutton–Chen potential for Al are: $\epsilon = 3.31477 \times 10^{-2}$ eV, $c = 16.399$, $a = 4.05$ Å, $m = 6$, $n = 7$. For the interphase potential we choose the parameter $\alpha = 0.48$ in Eq. (64).

The justification of the above approach is based on the argument that significant concentration of vacancy inside a damaged

interphase element will greatly affect electron density distribution. Therefore, we neglect its contribution in the colloidal crystal approximation. Based on the proposed AIZM model, a dynamic simulation of penetration/fragmentation of a polycrystalline aluminum cylinder through an aluminum plate is carried out in this example. The polycrystalline aluminum projectile is 1 mm in diameter and 3 mm in total length, and it impacts a square aluminum plate that has the dimension $5 \text{ mm} \times 5 \text{ mm} \times 0.2 \text{ mm}$ (width \times length \times thickness). The initial velocity of the projectile is: 4000 m/s, shown as Fig. 15. The shock wave induced by impact force propagates in both projectile as well as the target plate, which causes dynamic fracture phenomena in both bodies.

In this simulation, the bulk grains are represented by the tetrahedral element with various volumes and lattice orientations. Between grains, there is a wedge shaped interphase element that represents the grain boundary. The computational domain is discretized by 64,608 bulk elements and 124,820 interphase elements. The problem set-up and the finite element mesh are shown in Fig. 26. From Fig. 27, one can observe the progressive fragmentation of a high-speed projectile during and after penetrating the thin aluminum plate. Based on the authors' best knowledge, this is the first successful simulation of this problem by any numerical methods, including CZM, reported in the literature.

In this paper, we only briefly present a few preliminary results of AIZM simulation on high speed impact and fragmentation problems. An detailed report on how to use AIZM to simulate three-dimensional spall fracture and various fragmentation problems will be discussed in a separated paper [37].

7. Discussion

In this paper, we have reported a systematic study on the atomistic-based interphase zone model, and we have formulated and implemented a multiscale finite element formulation of AIZM. The proposed AIZM method is a single-physics coarse grained model that may be able to describe physics of solids in a broad spatial scales, from a hundred nanometers to mm scale. As shown in this paper, this method is capable of simulating strong discontinuities across a solid at nanoscale, such as micro-cracks and dislocations at small scales. Compared to conventional cohesive finite element method, the proposed AIZM model employs basic principles of colloidal physics and surface chemistry to determine the interface cohesive force, and it is exploiting the underneath atomistic structure to construct surface or interface cohesive relations.

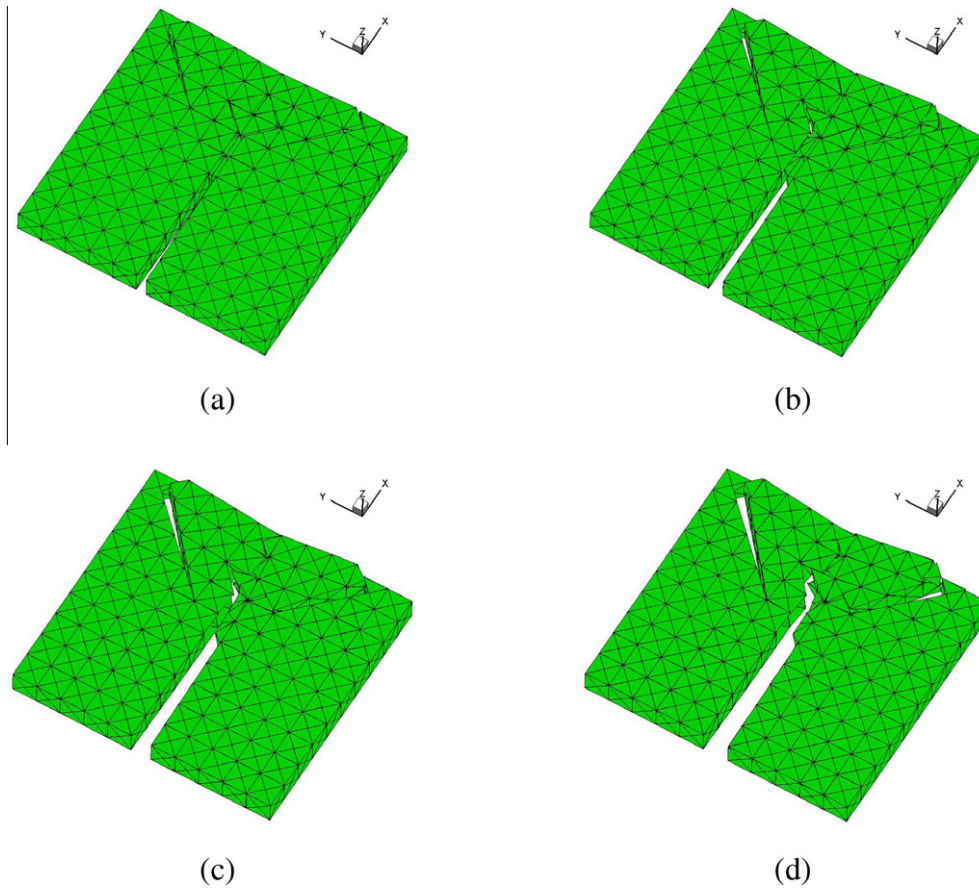


Fig. 25. Three-dimensional simulations of ductile fracture.

To do so, we first extend the Cauchy–Born rule to the effective deformation field of an interphase zone subject non-uniform deformation; and then we propose a novel concept of element (mesh) stacking fault energy that provides clear guidelines to simulate both ductile and brittle fractures.

The preliminary numerical results have shown that the proposed multiscale cohesive zone model may yield more accurate results than the conventional cohesive zone approach. In specific, this is because first we adopt an atomistically informed constitu-

tive relation; second both the normal and tangential cohesive surface potentials are derived from a single bulk depletion potential, and therefore they are consistent with each other, and in fact AIZM is applicable for arbitrary loading conditions without additional mix-mode fracture criterion, and third in the proposed AIZM method the bulk material properties and the material properties inside the interphase element are made consistent with each other, because the depletion potential is derived from the bulk atomistic potential.

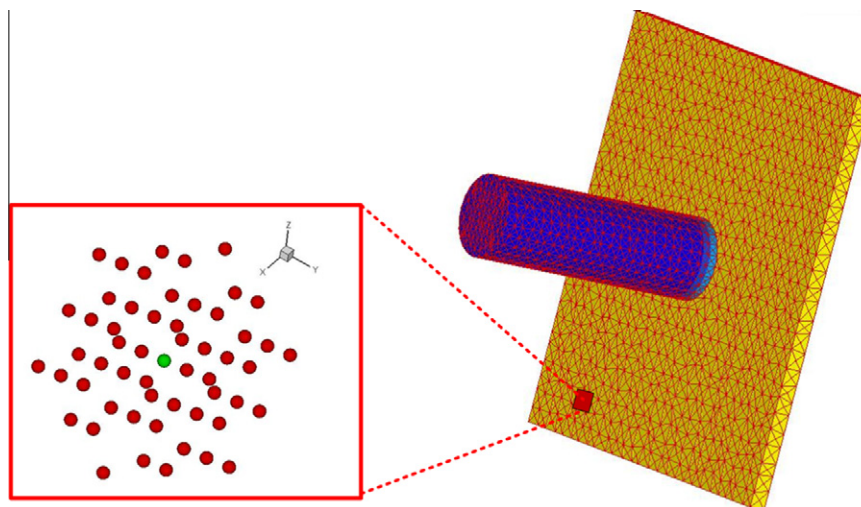


Fig. 26. AIZM mesh for aluminum projectile/target system with an EAM potential.

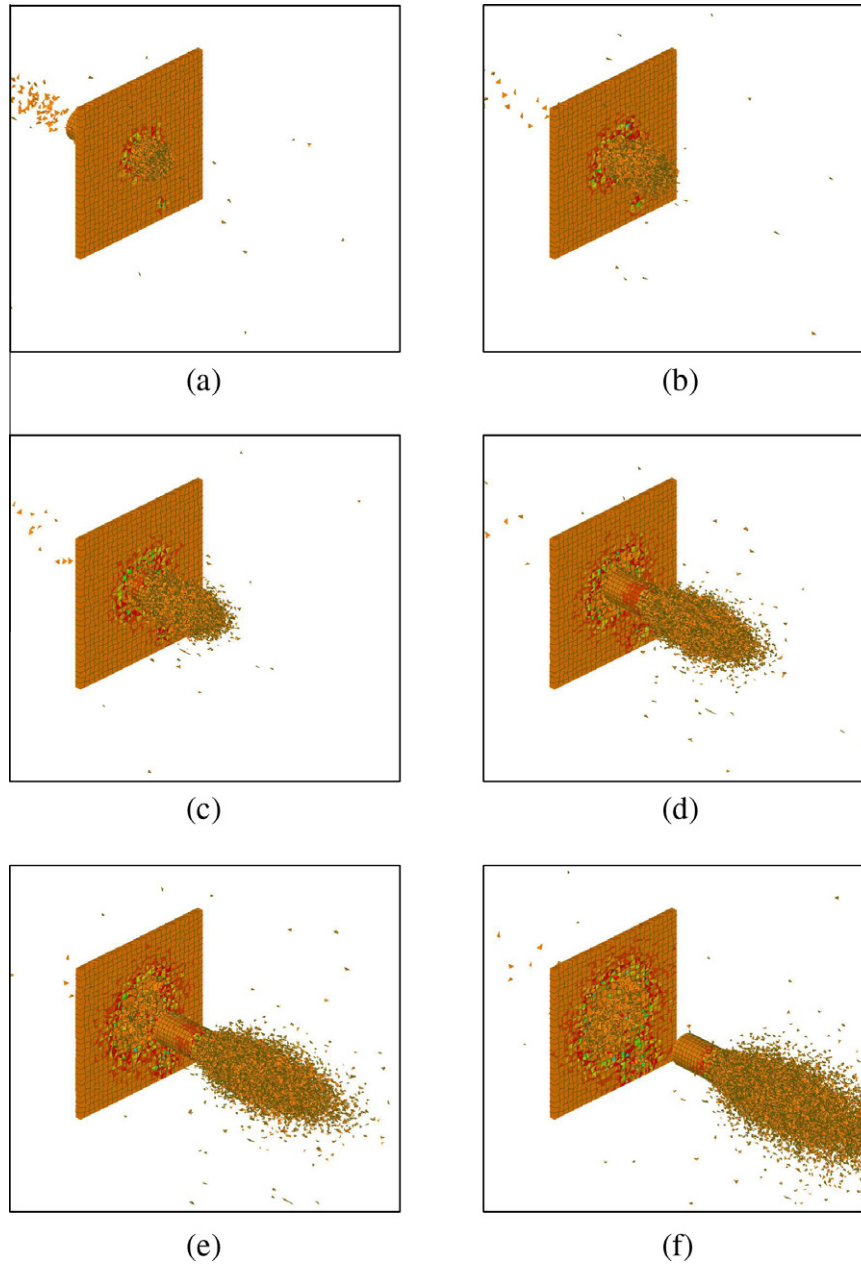


Fig. 27. Three-dimensional AIZM simulation of fragmentation of an aluminum projectile.

The justification for use of a finite thickness interphase zone and for use of the Cauchy–Born rule to the mean field in the interphase zone are based on the hypothesis that *most defects are multiscale entities*, so should be the interphase zone. Taking the crack as an example, except at initial stage of atomistic scale fracture, crack growth may be purely a cleavage surface separation; once the initial crack growth starts, it may grow into a depleted material zone, which involves with convolutions of many other types of defects such as voids, grain boundaries, slip lines, and surface separations. The microscale cleavage feature will be lost.

To be a truly multiscale method, one would expect a multiscale method transcendental across the scales. The real questions are:

1. Can AIZM model resolve cohesive length scale?
2. Can AIZM model resolve atomistic resolution?
3. How to choose R_0 ?

First, as mentioned before, the conventional CZM requires that $\ell_{fem} < \ell_{czm}$, and according to linear elastic theory [28],

$$\ell_{czm}(v=0) = \frac{9\pi}{32} \left(\frac{E}{1-\nu^2} \right) \frac{2\gamma}{\sigma_m^2},$$

where E is the Young's modulus, ν is the Poisson's ratio, and σ_m is the material strength. For $\sigma_m \sim E/10 - E/20 \rightarrow 10-70 \mu\text{m}$.

For AIZM modeling, the parameters E , γ , and σ_m can all be extrapolated from interphase atomistic potential. In fact, AIZM length scale is the shortest distance between two quadrature points. If we use one-point integration, AIZM length scale may become ℓ_{fem} , otherwise it is controlled by the spacing of quadrature points. In fact, one can introduce bubble functions in the interphase elements, and we may place several quadrature points in the longitudinal direction of the interface to increase accuracy of quadrature integration while avoiding shear locking.

For CZM, when $\ell_{fem} < \ell_{czm}$, it will have strong interaction between the cohesive zones [13], and this will not happen in AIZM.

This is because AIZM is not a cohesive zone model, and the interphase zone is also a special bulk element, and all the interaction between the elements are local; even though it may be interpreted as an atomistic-based cohesive zone model (for one-point integration case) in the sense of coarse-graining. In passing, we would like to point out that the multiple reduced integration algorithm always perform better than the one-point integration algorithm in general.

The second question and the third question are somewhat related, because in AIZM, R_0 is related to ℓ_{fem} . In practice, how to choose the thickness of the interphase zone depends on the requirements of the simulation problem itself, and it may range from a few nano-meters to sub-microns depending the specific type of defects that one wishes to simulate. Once we determine R_0 , we may then determine ℓ_{fem} based their ratio in AIZM formulation. Moreover, we have found that when we decrease R_0 to atomistic scale, we have to increase the ratio $R_0/\ell_{fem} \rightarrow \mathcal{O}(1)$. So far a nanoscale scale case that we have tested is the case in which R_0 equals about 5 atomic spacing. In this case, the hexagonal element among several interphase zone elements will become essential, and the detailed fine scale element configuration has to be carefully meshed with underneath lattice structure, in order to have a conforming fine scale finite element discretization. This is the fine scale limit of AIZM, which is more or less like a molecular dynamics simulation. In the fine scale limit of AIZM, additional information or constraints may be needed in determining R_0 and R_0/ℓ_{fem} ratio. An in-depth study of microscale limit of AIZM will be reported in a separate paper. Physically, almost all the defects have finite thickness, these include grain boundaries, phase boundaries, persistent slip bands (PSB), twin boundaries, etc., and they range from a few nanometers to sub-microns—that is the physical basis for the proposed atomistic-based interphase zone model.

Finally, one of the main advantages of AIZM is that this model can be easily incorporated into a con-current multiscale scheme with the molecular dynamics method by using the bridging scale approach e.g. [46]. In fact, the con-current coupling between AIZM model and MD has recently been achieved by the present authors [22]. A multiscale simulation of a moving screw dislocation has been carried out there, which allows a dislocation passing through different scales.

Acknowledgements

This work is supported by a grant from NSF (Grant No. CMMI-0800744) and a grant from Army Research Office, which are greatly appreciated.

References

- [1] T. Antoun, L. Seaman, D.R. Curran, G.I. Kanel, Spall Fracture (Shock Wave and High Pressure Phenomena), Springer, 2003.
- [2] G.I. Barrenblatt, The mathematical theory of equilibrium of cracks in brittle fracture, *Adv. Appl. Mech.* 7 (1962) 55–129.
- [3] T. Belytschko, An overview of semidiscretization and time integration procedure, in: T. Belytschko, T.J.R. Hughes (Eds.), *Computational Methods for Transient Analysis*, North-Holland, Amsterdam, 1983, pp. 1–65.
- [4] T. Belytschko, J.-S. Ong, W.K. Liu, J.M. Kennedy, Hourglass control in linear and nonlinear problems, *Comput. Methods Appl. Mech. Engrg.* 43 (1984) 251–276.
- [5] T. Belytschko, W.-K. Liu, B. Moran, *Nonlinear Finite Elements for Continua and Structures*, Wiley, John & Sons, Chichester, Wset Sussex, England, 2000.
- [6] A. Braides, A.J. Lew, M. Ortiz, Effective cohesive behavior of layers of interatomic planes, *Arch. Ration. Mech. Anal.* 180 (2006) 151–182.
- [7] M.J. Buehler, F.F. Abraham, H. Gao, Hyperelasticity governs dynamic fracture at a critical length scale, *Nature* 426 (2003) 141–146.
- [8] Y. Chen, J.D. Lee, Atomistic formulation of a multiscale field theory for nano/micro solids, *Philos. Mag.* 85 (2005) 4095–4126.
- [9] J. Chen, X. Wang, H. Wang, J.D. Lee, Multiscale modeling of dynamic crack propagation, *Engrg. Fract. Mech.* 77 (2010) 736–743.
- [10] J.D. Clayton, Modeling dynamic plastic and spall fracture in high-density polycrystalline alloys, *Int. J. Solids Struct.* 42 (2005) 4613–4640.
- [11] M.S. Daw, M.I. Baskes, Embedded-atom method: derivation and application to impurities, surfaces, and other defects in metals, *Phys. Rev. B* 29 (1984) 6443–6453.
- [12] D.S. Dugdale, Yielding of steel sheets containing slits, *J. Mech. Phys. Solids* 8 (1960) 100–104.
- [13] M.L. Falk, A. Needleman, J.R. Rice, A critical evaluation of cohesive zone models of dynamic fracture, *J. Phys. IV France* 11 (2001) 43–50.
- [14] H. Gao, P. Klein, Numerical simulation of crack growth in an isotropic solid with randomized internal cohesive bonds, *J. Mech. Phys. Solids* 46 (1988) 87–218.
- [15] M. He, S. Li, An embedded atom hyperelastic constitutive model and multiscale, *Comput. Mech.* 49 (2012) 337–355.
- [16] R. Hill, On constitutive macro-variables for heterogeneous solids at finite strain, *Proc. Roy. Soc. Lond. A* 326 (1972) 131–147.
- [17] M.F. Horstemeyer, M.I. Baskes, V.C. Prantil, J. Philliber, A multiscale analysis of fixed-end simple shear using molecular dynamics, crystal plasticity, and a macroscopic internal state variable theory, *Model. Simul. Mater. Sci. Engrg.* 11 (2003) 265–286.
- [18] T.J.R. Hughes, R. Talor, J. Sackman, A. Curnier, W. Kamoknukulchai, A finite element method for a class of contact-impact problem, *Comput. Methods Appl. Mech. Engrg.* 8 (1976) 249–276.
- [19] T.J.R. Hughes, *The Finite Element Method: Linear Static and Dynamic Finite Element Analysis*, Prentice Hall, 1987.
- [20] J. Israelachvili, *Intermolecular Surface & Forces*, second ed., Academic Press, 1992.
- [21] J.D. Lee, X. Wang, Y. Chen, Multiscale material modeling and its application to a dynamic crack propagation problem, *Theor. Appl. Fract. Mech.* 51 (2009) 33–40.
- [22] S. Li, X. Liu, A. Agrawal, A.C. To, The perfectly matched multiscale simulations for discrete systems: Extension to multiple dimensions, *Phys. Rev. B* 74 (2006) 045418.
- [23] S. Li, G. Wang, *Introduction to Micromechanics and Nanomechanics*, World Scientific Publication Inc., Singapore, 2008.
- [24] X. Liu, S. Li, N. Sheng, A cohesive finite element for quasi-continua, *Comput. Mech.* 42 (2008) 543–553.
- [25] G. Lu, E.B. Tadmor, E. Kaxiras, From electrons to finite elements: a concurrent multiscale approach for metals, *Phys. Rev. B* 73 (2006). Article No. 024108.
- [26] D.S. Markus, T.J.R. Hughes, Mixed finite element methods Reduced and selective integration techniques: a unification of concepts, *Comput. Methods Appl. Mech. Engrg.* 15 (1978) 63–81.
- [27] N. Moës, T. Belytschko, Extended finite element method for cohesive crack growth, *Engrg. Fract. Mech.* 69 (2002) 813–833.
- [28] J.W. Morrissey, J.R. Rice, Crack front waves, *J. Mech. Phys. Solids* 46 (1998) 467–487.
- [29] F. Nabarro, Mathematical theory of stationary dislocations, *Adv. Phys.* 1 (1952) 269–394.
- [30] O. Nguyen, M. Ortiz, Coarse-graining and renormalization of atomistic binding relations and universal macroscopic cohesive behavior, *J. Mech. Phys. Solids* 50 (2002) 1727–1741.
- [31] M. Ortiz, A. Pandolfi, Finite-deformation irreversible cohesive elements for three-dimensional crack-propagation analysis, *Int. J. Numer. Methods Engrg.* 44 (1999) 1267–1282.
- [32] S. Pelaez, P. Garcia-Mochales, P.A. Serena, A comparison between EAM interatomic potentials for Al and Ni: from bulk systems to nanowires, *Phys. Stat. Sol. (A)* 203 (6) (2006) 1248–1253.
- [33] J. Qian, S. Li, Application of multiscale cohesive zone model to simulate fracture in polycrystalline solids, *ASME J. Engrg. Mater. Technol.* 133 (2011). No. 011010.
- [34] H.S. Park, E.G. Karpov, W.K. Liu, P.A. Klein, The bridging scale for three-dimensional atomistic/continuum coupling, *Philos. Mag.* 85 (2005) 79–113.
- [35] R. Peierls, The size of a dislocation, *Proc. Roy. Soc. Lond.* 52 (1940) 34–37.
- [36] K. Park, G.H. Paulino, J.R. Roesler, A unified potential-based cohesive model of mixed-mode fracture, *J. Mech. Phys. Solids* 57 (2009) 891–908.
- [37] B. Ren, S. Li, A three-dimensional atomistic-based interphase finite element simulation of fragmentation in polycrystalline solids, *Int. J. Numer. Methods Engrg.*, submitted for publication.
- [38] J.R. Rice, R.M. Thomson, Ductile versus brittle behaviour of crystals, *Philos. Mag.* 29 (1974) 73–97.
- [39] J.R. Rice, Dislocation nucleation from a crack tip: an analysis based on the Peierls concept, *J. Mech. Phys. Solids* 40 (1992) 239–271.
- [40] J.R. Rice, G.E. Beltz, The activation energy for dislocation nucleation at a crack, *J. Mech. Phys. Solids* 42 (1994) 333–360.
- [41] R. Sauer, S. Li, A contact mechanics model for quasi-continua, *Int. J. Numer. Methods Engrg.* 71 (2007) 931–962.
- [42] P. Schall, I. Cohen, D.A. Weitz, F. Spaepen, Visualizing dislocation nucleation by indenting colloidal crystals, *Nature* 440 (2006) 319–323.
- [43] S. Suresh, Colloid model for atoms, *Nat. Mater.* 5 (2006) 253–254.
- [44] G.I. Taylor, Plastic strain in metals, *J. Inst. Metals* 62 (1938) 307–324.
- [45] R. Tian, S. Chan, S. Tang, A.M. Kopacz, J.-S. Wang, H.-J. Jou, L. Siad, L.-E. Lindgren, G.B. Olson, W.-K. Liu, A multiresolution continuum simulation of the ductile fracture process, *J. Mech. Phys. Solids* 58 (2010) 1681–1700.
- [46] G.J. Wagner, W.K. Liu, Coupling of atomic and continuum simulations using a bridging scale decomposition, *J. Comput. Phys.* 190 (2003) 249–274.

- [47] G.N. Wells, L.J. Sluys, A new method for modelling cohesive crack using finite elements, *Int. J. Numer. Methods Engrg.* 50 (2001) 2667–2682.
- [48] S. Xiao, W. Yang, A temperature-related homogenization technique and its implementation in the meshfree particle method for nanoscale simulations, *Int. J. Numer. Methods Engrg.* 69 (2007) 2099–2125.
- [49] X.-P. Xu, A. Needleman, Numerical simulations of fast crack growth in brittle solids, *J. Mech. Phys. Solids* 42 (1994) 1397–1434.
- [50] X.W. Zeng, S. Li, A multiscale cohesive zone model and simulations of fractures, *Comput. Methods Appl. Mech. Engrg.* 199 (2010) 547–556.